

Pressure Regulated Formation of Molecular Clouds and Stars: The case of the Milky Way

José Franco,¹★, Aldo Rodríguez-Puebla,¹ Javier Ballesteros-Paredes², and Manuel Zamora-Avilez³

¹Universidad Nacional Autónoma de México, Instituto de Astronomía, A. P. 70-264, 04510, Ciudad de México, México

²Universidad Nacional Autónoma de México, Instituto de Radioastronomía y Astrofísica, Antigua Carretera a Pátzcuaro 8701, Ex-Hda, San José de la Huerta 58089 Morelia, Michoacán, México

³Instituto Nacional de Astrofísica, Óptica y Electrónica, Luis E. Erro 1, 72840 Tonantzintla, Puebla, México

arXiv:2509.12128v2 [astro-ph.GA] 3 Oct 2025

Accepted XXX. Received YYY; in original form ZZZ

ABSTRACT

We present a steady-state analytical model for pressure-regulated formation of molecular clouds (MC) and stars (SF) in gaseous galactic disks and apply it to the Milky Way (MW). MC formation depends on midplane interstellar pressure P_{ISM} and metallicity Z , and for galactocentric distances $R \gtrsim 5$ kpc, $P_{\text{ISM}}(R)$ scales approximately linearly with molecular gas surface density $\Sigma_{\text{mol}}(R)$. The molecularization of the cold neutral medium (CNM) is due to the opacity of small dust grains that protect the center of the cloud from dissociating radiation when the column density is $\Sigma_d \geq 5 (Z_{\odot}/Z) M_{\odot} \text{ pc}^{-2}$. The H₂ formation rate per hydrogen atom is $F \sim 10^{-15} (P_{\text{ISM}}/P_{\odot}) T_{100}^{-1/2} \text{ s}^{-1}$, and the corresponding formation rate per unit area is $\dot{\Sigma}_{\text{mol}}^+ \sim 5 \times 10^{-2} (P_{\text{ISM}}/P_{\odot}) T_{100}^{-1/2} M_{\odot} \text{ kpc}^{-2} \text{ yr}^{-1}$, where P_{\odot} is the pressure at the solar circle and $T_{100} = T/100$ K is the temperature of the cloud. In equilibrium, this equals the molecular gas destruction rate $\dot{\Sigma}_{\text{mol}}^-$ due to SF. Self-gravity sets in when the column density of a cloud reaches $\Sigma_{\text{sg}} = \Sigma_{\text{sg},\odot} (P_{\text{ISM}}/P_{\odot})^{1/2}$, with $\Sigma_{\text{sg},\odot} \sim 30 M_{\odot} \text{ pc}^{-2}$. Given the distribution of $P_{\text{ISM}}(R)$ and $Z(R)$ in the MW, the SF process at $5 \lesssim R \lesssim 11$ kpc follows a two-step track: first, MCs form from CNM gas and then they form stars when self-gravity sets in. The resulting SFR surface density is $\Sigma_{\text{SFR}}(R) \approx (1.6 - 4) \times 10^{-3} (P_{\text{ISM}}/P_{\odot}) M_{\odot} \text{ kpc}^{-2} \text{ yr}^{-1}$ with an average final SF efficiency of $\epsilon_{\text{sf}} \sim (3 - 8) \times 10^{-2}$.

Key words: ISM: clouds – H II regions – galaxies: star formation – local interstellar matter

1 INTRODUCTION

Star formation remains an unsolved problem in astrophysics; although we have a general framework for how stars form, many of the specific mechanisms and outcomes remain poorly understood (see reviews Kennicutt & Evans 2012; Sánchez 2020; Schinnerer & Leroy 2024). Key open questions include issues from what determines the formation rate of star-forming clouds to how the mass of these clouds is ultimately distributed among stars. Thus, one of the central unresolved questions is how the physical processes act in concert with the system parameters to regulate the molecular cloud and star formation rates, along with the resulting star formation efficiency.

Almost seven decades ago, Schmidt (1959) proposed that the rate of star formation should scale as a power of the gas density. Although several studies in the 1970s and early 1980s attempted to quantify this relationship (i. e., Sanduleak 1969; Madore et al. 1974; Talbot 1980), it was not until the late 1980s and 1990s that a clear power-law correlation was established between the surface density of star formation and the surface density of interstellar gas (Buat et al. 1989; Kennicutt 1989, 1998, see also Kennicutt & De Los Reyes 2021 for recent determinations).

Numerous studies in the early 2000s further investigated this correlation, which is usually referred to as the Kennicutt-Schmidt relation, consistently finding similar results but with different gas tracers. These efforts included analyses of the radial dependence of the star formation rate on the total gas surface density in galaxies (e.g., Wong & Blitz 2002; Blitz & Rosolowsky 2004, 2006; Sánchez 2020), measurements of the star formation rate as a function of the mass in dense gas in unresolved galaxies (e.g., Gao & Solomon 2004), and studies of galaxies resolved at kiloparsec scales Bigiel et al. (2008). Interestingly, a variety of correlations have been found between the measurements of the star formation rate with molecular gas mass and interstellar pressure (e.g., Elmegreen 1993a; Elmegreen & Paravano 1994; Wong & Blitz 2002; Blitz & Rosolowsky 2004, 2006; Fisher et al. 2017; Sánchez 2020; Barrera-Ballesteros et al. 2021; Sun et al. 2023; Ellison et al. 2024, For comprehensive reviews of these works, see, e.g., Kennicutt & Evans 2012; Sánchez 2020; Schinnerer & Leroy 2024).

Various theoretical models have been proposed to explain the observed correlations; for example, Elmegreen (2002) sought to explain the Kennicutt-Schmidt relation by assuming that the galactic disks maintain an approximately constant scale height and that the gas is undergoing gravitational collapse. Other studies have interpreted the correlation in terms of large-scale gravitational instabilities, particu-

★ E-mail: pepe@astro.unam.mx

larly with the Toomre (1964) criterion (e.g., Li et al. 2005), with turbulent support of the interstellar medium (e.g., Krumholz & McKee 2005; Padoan et al. 2012; Kim et al. 2021), or with sustained gas accretion into molecular clouds (Zamora-Avilés 2014). Several authors have also emphasized the critical role of self-gravity in regulating star formation (e.g., Krumholz et al. 2012; Elmegreen 2018), and the role of interstellar pressure in regulating the properties of the interstellar gas and hence star formation (e.g., Elmegreen 1993b; Elmegreen & Parravano 1994; Wong & Blitz 2002; Blitz & Rosolowsky 2004, 2006; Ostriker et al. 2010). More recently, Ballesteros-Paredes et al. (2024) proposed that the diversity of observational correlations reported in the literature may arise naturally from the gravitational collapse of dense gas, with the variations resulting from the specific biases inherent in each observational methodology.

An idea that has received more attention is the self-consistent model proposed by Ostriker et al. (2010), which has been further developed in a series of articles that include numerical simulations (see Kim et al. 2011; Kim & Ostriker 2017; Ostriker & Kim 2022). The model assumes that star formation is self-regulated, where the main source of energy for the interstellar medium comes from recently formed stars, keeping the ionization and temperature of the gas components in balance, along with their velocity dispersions and corresponding scale heights. The resulting star formation rate then compensates for the energy and momentum losses of the system, and the gaseous disk is maintained in a stable dynamical equilibrium. With these assumptions, the star formation rate per unit area is the one required to provide support against the weight of a column density of gas, and, as a result, the rate becomes proportional to the disk pressure at midplane. For pressures below $\log(P_{\text{ISM}}/k) \sim 5.5$, this result is in accordance with the observationally derived linear correlation between star formation rates and the pressures obtained in several surveys of nearby galaxies (Leroy et al. 2008; Sun et al. 2020; Barrera-Ballesteros et al. 2021; Ellison et al. 2024). For higher pressures, the correlation is no longer linear, becomes shallower, and models with variations that include the possibility of radial gas inflows as an additional source of kinetic energy for the gas have been proposed by Krumholz et al. (2018).

One issue that remains unanswered in these and other models is how the formation rates of molecular gas and stars are entangled and regulated by the overall system properties and how they are distributed along the galactic disk. Here we address these and other related questions with a simplified steady-state analytical model for a gaseous galactic disk and apply it to the Milky Way (MW). We derive the dependence of molecular cloud formation and star formation as a function of two basic parameters of the system, the interstellar pressure in the midplane, P_{ISM} , and its metallicity, Z . In Section 2 we use the available data to obtain the interstellar pressure in the midplane as a function of the galactocentric radius. Then, assuming that the population of cold diffuse clouds are the precursors of molecular clouds, in Section 3 we derive the radial variation of the threshold conditions for the formation of molecular clouds, the formation rate of H_2 on dust grains as a function of P_{ISM} , and the formation rate of molecular gas per unit surface along the disk. In Section 4, the threshold conditions for self-gravity are presented, and we obtain the star formation rate per unit surface along with its corresponding star formation efficiency. The model is simple and basic but provides a broad picture of the role that pressure and metallicity play in the regulation of the formation process of both molecular gas and stars.

2 SYSTEM PRESSURE AND DIFFUSE CLOUDS IN THE MILKY WAY

2.1 Pressure and density of diffuse clouds

The interstellar pressure in the disk of a spiral galaxy is due to the weight of the column density of its interstellar gas. For a multi-component disk (with gaseous, stellar, and dark-matter components), locally plane-parallel, in rotational equilibrium and in steady state, Poisson's equation in cylindrical coordinates,

$$\frac{1}{r} \frac{\partial}{\partial r} \left(r \frac{\partial \Phi}{\partial r} \right) + \frac{1}{r^2} \frac{\partial^2 \Phi}{\partial \theta^2} + \frac{\partial^2 \Phi}{\partial z^2} = -4\pi G \rho_{\text{tot}}, \quad (1)$$

has a simple solution for the pressure of a thin gaseous disk at any given galactocentric radius: the gravitational acceleration due to the gravitational potential Φ depends only on z , is perpendicular to the disk, and the interstellar pressure is given by

$$\frac{dP_{\text{ISM}}}{dz} = -\rho_g g_z, \quad (2)$$

where G is the gravitational constant, ρ_{tot} is the total mass volume density, ρ_g is the gas mass volume density, and g_z is the local gravitational acceleration along the z axis. The pressure at midplane along the disk is then

$$P_{\text{ISM}} = \frac{\pi G}{2} \Sigma_{\text{gas}} \Sigma_{\text{tot}} = \frac{\pi G}{2} \Sigma_{\text{gas}} [\Sigma_{\text{gas}} + (\Sigma_* + \Sigma_{\text{dm}})] \\ = \frac{\pi G}{2} (\Sigma_{\text{gas}}^2 + \Omega), \quad (3)$$

where Σ_{gas} is the surface mass density of the three gaseous components (molecular, atomic, and ionized), Σ_{tot} is the total surface mass density, including the contribution of gas, stars (Σ_*) and dark matter (Σ_{dm}), and $\Omega = \Sigma_{\text{gas}} (\Sigma_* + \Sigma_{\text{dm}})$. This steady-state pressure controls the average properties of the ambient gas, and any impulsive transient event (such as the injection of energy from new stellar clusters, the passage of spiral arms, the action of torques driving radial gas inflows, or collisions with high-velocity clouds) can increase the local ISM pressure momentarily, but the system relaxes back to its base value after a crossing time of the perturbed region.

The first term on the right-hand side of Eq. (3) is proportional to Σ_{gas}^2 and represents the pressure component due to the gas's own self-gravity. The second term, proportional to Ω , is the dominant component along spiral disks and is due to the gravitational field provided by stars and dark matter. At the solar circle, it is 7 times higher than that of the gas self-gravity (see below), and it has been approximated in two different ways to account for the difference in scale heights of gas and stars in external galaxies (but neglecting the contribution from dark matter). In one case, assuming hydrostatic equilibrium, the ratio of gas and star velocity dispersions, $\sigma_{\text{gas}}/\sigma_{*,z}$, has been used to approximate this difference (Elmegreen 1989; Elmegreen & Parravano 1994; Wong & Blitz 2002),

$$\Omega_H \approx \Sigma_{\text{gas}} \frac{\sigma_{\text{gas}}}{\sigma_{*,z}} \Sigma_*. \quad (4)$$

The resulting total pressure is usually termed the hydrostatic equilibrium pressure P_H . In the second case, the energy input from star formation is used to maintain the velocity dispersion and the scale height of the ambient gas. The stellar mass is assumed to be distributed in an isothermal disk (with average volume density ρ_*), where the stellar scale height h_* and the stellar velocity dispersion are related by $\sigma_{*,z} \approx (2\pi G \Sigma_* h_*)^{1/2}$. These assumptions give (see Blitz & Rosolowsky 2004; Ostriker et al. 2010; Kim et al. 2011; Sun et al. 2020),

$$\Omega_{DE} \approx \frac{2}{\pi G} \Sigma_{\text{gas}} \sigma_{\text{gas},z} \sqrt{2G\rho_*}, \quad (5)$$

and the corresponding pressure is called the dynamical equilibrium pressure P_{DE} . Note that these definitions differ only by a constant, $\Omega_{DE}/\Omega_H = (16/\pi)^{1/2}$, and the resulting values of the dynamical equilibrium pressure are approximately two times higher than those of the hydrostatic equilibrium (see Table 2 in Fisher et al. 2019). Our definition of interstellar pressure includes the contribution of dark matter and, except for a factor very close to unity (1.05), is equal to the one termed gravitational pressure P_{grav} by Wilson et al. (2019) and Molina et al. (2020).

Regardless of these definitions, the weight of the gas is largely supported by the volume-averaged thermal pressure of the gaseous disk and the nonthermal pressures ascribed to Galactic cosmic rays, turbulent velocities and magnetic fields, all of which seem to have similar energy densities in the solar neighborhood and are generally assumed to be in equipartition along the disk (see Boulares & Cox 1990; Ferrière 2001; Cox 2005; Grenier et al. 2015; Commerçon et al. 2019; Crocker et al. 2021). However, a key question for understanding the possible role of nonthermal pressures in the formation of molecular clouds and stars is how their ambient energy densities are coupled and transmitted to existing diffuse clouds, whose internal pressures must be in balance with the external medium. This is a relevant issue because the thermal pressures of diffuse clouds, which are their best known physical properties, are clearly below the external pressures (see Jenkins & Tripp 2001).

Cosmic rays and magnetic fields are closely coupled, but the details of the collective trapping and coupling of cosmic rays in clouds depend on the diffusion coefficient along the magnetic field lines (which in turn depends on the cosmic ray energies and the strength of the turbulent component of the magnetic field). Individually, they provide ionization and heating and drive the chemistry in dark clouds, but their collective effects can influence the structure and evolution not only of the cloud population but also of the diffuse ionized medium and may even launch galactic winds (see e.g., Grenier et al. 2015; Girichidis et al. 2016; Commerçon et al. 2019; Armillotta et al. 2021; Hopkins et al. 2020; Brugallé et al. 2025; Rodríguez Montero et al. 2024; Barreto-Mota et al. 2024). In particular, numerical simulations of cosmic ray feedback in turbulent and magnetized interstellar media indicate that, when the diffusion coefficient parallel to the magnetic field is below a critical value $D_{\text{crit}} \sim 10^{24} - 10^{25} \text{ cm}^2 \text{ s}^{-1}$, they can pair with the evolution of diffuse clouds, providing effective internal support and preventing them from reaching denser states (Commerçon et al. 2019). As the value of the diffusion coefficient increases, the coupling is less and less efficient, letting clouds reach denser and cooler stages. For Galactic cosmic rays at around 1 GeV (the peak of their energy spectrum; Grenier et al. 2015) the diffusion coefficient is about $10^{28} \text{ cm}^2 \text{ s}^{-1}$ (Ptuskin et al. 2006), well above the critical value, and in circum-galactic media it can reach values of $\sim 3 \times 10^{29} \text{ cm}^2 \text{ s}^{-1}$ (Hopkins et al. 2020). A recent study with “mirror diffusion” (cosmic ray scattering at large pitch angles that can produce a secondary acceleration in turbulent molecular clouds; see Lazarian et al. 2011) shows that the corresponding diffusion coefficient tends to values around $10^{27} \text{ cm}^2 \text{ s}^{-1}$ (Barreto-Mota et al. 2024), also above the critical value. These results, then, imply that the coupling with the cold neutral cloud population of the MW disk is weak, which is in line with the fact that our Galaxy displays a bistable diffuse neutral medium (see Wolfire et al. 2003; Commerçon et al. 2019). Here we assume that cosmic rays do not collectively couple with the cold neutral medium (CNM) of the MW and also that the total internal pressures of cold diffuse clouds are in equilibrium with their external ambient pressure $P_{\text{cl}} = P_{\text{ISM}}$.

Magnetic fields and turbulent flows are important in structuring the interstellar medium and reducing the efficiency of star forma-

tion, as clearly shown in a series of works with detailed numerical simulations displaying their effects when acting in concert with self-gravity and stellar feedback (e.g., Federrath & Klessen 2012, 2013; Federrath 2013, 2016). A recent study by Seta & McClure-Griffiths (2025) shows that the observed average values of the magnetic and turbulent energy densities along the line of sight of different sources in our Galaxy, E_{mag} and E_{kin} , follow a power law relationship $E_{\text{mag}} \propto E_{\text{kin}}^{\alpha_m}$, where the exponent α_m varies between 0.9 and 0.64. This implies that magnetic fields do not simply scale with gas density, as is usually assumed, but also with the local velocity field, making it difficult to know the actual coupling of these energy densities with the cold neutral phase. This complication also makes it difficult to assess their possible role in the formation of dense molecular clouds. However, as previously discussed, the thermal energy densities of diffuse clouds are better known than any other properties of clouds, and their values are generally a factor of 4 to 8 below the total ambient pressure (see e.g., Boulares & Cox 1990; Jenkins & Tripp 2001; Wolfire et al. 2003; Cox 2005; Jenkins 2009). Thus, as a reasonable approximation, we set the total CNM cloud pressure in terms of its thermal pressure and assume that $P_{\text{cl}} \sim 6P_{\text{th}} = 6n_{\text{cl}}kT_{\text{eff}}$, where k is the Boltzmann constant and T_{eff} is the average effective cloud temperature. With this assumption, the contribution of nonthermal pressures is implicitly included, and the average cloud volume densities can be approximated as

$$n_{\text{cl}} \approx \frac{P_{\text{ISM}}}{6 kT_{\text{eff}}}. \quad (6)$$

2.2 Radial distributions in the Milky Way

The MW has a boxy peanut-shaped bulge and a stellar bar whose major axis is estimated to be at an angle with the line of sight between 23° and 45° (see Dwek et al. 1995; Mosenkov et al. 2021, and references therein). The determinations of the radius of the bar major axis range from 1 to 4 kpc (see Freudenreich 1998; Zoccali & Valenti 2024, and references therein), whose effects are clearly present up to 4 kpc. The location of the solar circle is estimated to be within 7.5 and 8.4 kpc of the Galactic center (e.g., Zhu & Shen 2013; Francis & Anderson 2014; Reid et al. 2019), and for simplicity we set $R_\odot = 8$ kpc.

Here we will exclude the bulge zone and restrict discussions of the radial distributions outward of 4 kpc, where the rotation curve becomes approximately flat (McGaugh et al. 2016), and the gaseous disk can be considered thin, locally plane-parallel, and in rotational equilibrium. With regard to the dark matter component, which is supposed to be distributed in a spherical halo (Navarro et al. 1997), it may introduce a gravitational radial component along the disk, but we will assume that it is small compared to the total z component of the gravitational acceleration. The data compilations for the solar neighborhood indicate its presence in the disk (e.g., Bienaymé et al. 2014; McKee et al. 2015; Kramer & Randall 2016a,b, see Cheng et al. 2024 for a recent discussion of this issue), and its contribution has been included in the determinations of the total mass surface densities Σ_{tot} (gas, stars, and dark matter).

The derivations of the total surface gas mass densities in the solar circle $\Sigma_{\text{gas}}(R_\odot)$, range from 7 to $13 M_\odot \text{ pc}^{-2}$, while the total mass surface density integrated up to approximately 1 kpc above the mid-plane is about $\Sigma_{\text{tot}}(R_\odot, |z| \lesssim 1 \text{ kpc}) \approx 68 M_\odot \text{ pc}^{-2}$ (see Romano et al. 2000; Bovy & Rix 2013; Flynn et al. 2006; Kalberla & Dedes 2008; Pineda et al. 2013; Bienaymé et al. 2014; McKee et al. 2015; Kramer & Randall 2016b; Marasco et al. 2017; Miville-Deschénes et al. 2017b; Cheng et al. 2024). For the surface density of the different

gas components, we use $1.5 M_{\odot} \text{ pc}^{-2}$ for the molecular gas (Miville-Deschénes et al. 2017b), $5 M_{\odot} \text{ pc}^{-2}$ for the atomic gas and $2 M_{\odot} \text{ pc}^{-2}$ for the Reynolds ionized layer (Kramer & Randall 2016b). This gives a conservative value of $\Sigma_{\text{gas}}(R_{\odot}) \approx 8.5 M_{\odot} \text{ pc}^{-2}$. Our choice for the surface density of the total mass is $\Sigma_{\text{tot}}(R_{\odot}) \approx 68 M_{\odot} \text{ pc}^{-2}$ because its integration coincides with the scale height of the Reynolds layer (e.g., Reynolds et al. 1977; Reynolds 1993), which is approximately 1 kpc and, for simplicity, we omit the specification that the integration of the total mass is up to $|z| \sim 1$ kpc. With these values, the total interstellar pressure in the solar neighborhood is approximately $P_{\odot} \approx 3 \times 10^{-12} \text{ dyn cm}^{-2}$, or $P_{\odot}/k \approx 2 \times 10^4 \text{ cm}^{-3} \text{ K}$, which is in the range of values inferred for the total pressure at the solar circle, $(2 - 4) \times 10^{-12} \text{ dyn cm}^{-2}$ (Boulares & Cox 1990; Ferrière 2001; Cox 2005).

With respect to radial distributions, Bovy & Rix (2013) analyzed the total surface mass density for galactocentric radii from 4.5 to 9 kpc. Their modeled MW disk mass, within 1.1 kpc from the midplane, follows an exponential distribution with a scale length of 2.5 kpc and, as mentioned above, the total surface mass density at the solar circle is $68 M_{\odot} \text{ pc}^{-2}$. The contribution of the stellar component is $\sim 40 M_{\odot} \text{ pc}^{-2}$, resulting in a stellar to total mass ratio of ~ 0.6 . These values are similar to those found by Bienaymé et al. (2014), and we assume that the radial distribution of Σ_{tot} can be extrapolated to a galactocentric radius of ~ 14 kpc,

$$\Sigma_{\text{tot}}(R) \approx 68 \exp\left(\frac{R_{\odot} - R}{2.5 \text{ kpc}}\right) M_{\odot} \text{ pc}^{-2}. \quad (7)$$

The surface gas density in the MW has a peak at the Galactic center and a second peak at the molecular ring at about 4 kpc, then decreases monotonically afterwards, with several peaks associated with the presence of spiral arms (Kalberla & Dedes 2008; Kramer & Randall 2016b; Pineda et al. 2013; Marasco et al. 2017; Miville-Deschénes et al. 2017b). With respect to each specific gas component, the distribution of the surface mass densities of H_2 derived by Roman-Duval et al. (2010) covers the inner MW, while Kramer & Randall (2016b) covers the Galactic radii interval from 4 to 14 kpc and the compilation by Miville-Deschénes et al. (2017b) extends it to almost $R = 20$ kpc. The calibration and slopes of the radial distribution outside 5 kpc display several differences (see, Spilker et al. 2021), but for simplicity we use the more extended and explicitly stated exponential fit with the radial scale length of 2 kpc of Miville-Deschénes et al. (2017b), whose value at the location of the Sun is $\Sigma_{\text{H}_2}(R_{\odot}) \approx 1.5 M_{\odot} \text{ pc}^{-2}$. Thus, we approximate the surface density of the molecular gas mass outside 4 kpc with

$$\Sigma_{\text{H}_2}(R) \approx 1.5 \exp\left(\frac{R_{\odot} - R}{2 \text{ kpc}}\right) M_{\odot} \text{ pc}^{-2}. \quad (8)$$

Regarding the surface mass density of the atomic gas, it has several components with a warm component reaching heights of 400 pc above the midplane (see Dickey & Lockman 1990; Ferrière 2001; Cox 2005), and its radial distribution is almost flat up to 12 kpc, with most reported values ranging from 4 to $6 M_{\odot} \text{ pc}^{-2}$ (note that Kalberla & Dedes 2008 report a value of $10 M_{\odot} \text{ pc}^{-2}$, but this is well above the rest of the estimates; see the discussions by Kalberla & Dedes 2008 and Marasco et al. 2017). Outside 13 kpc, it displays an exponential decrease with a radial scale length of 3.5 kpc. So, we use a constant value of about $\Sigma_{\text{HI}} = 5 M_{\odot} \text{ pc}^{-2}$ up to 13 kpc, and then assume the outward exponential decrease described by Kalberla & Dedes (2008). Regarding the diffuse and ionized Reynolds layer (e.g., Reynolds et al. 1977; Reynolds 1993), it extends up to about 1 kpc from the midplane and appears to have a flat distribution along the disk with a value of $2 M_{\odot} \text{ pc}^{-2}$ (see Kramer & Randall 2016b). Its

presence is prevalent as an important extraplanar component in many other galaxies, sometimes extending several kpc above the main disk (e.g., Dettmar 1990; Collins et al. 2000; Vale Asari & Stasińska 2021). Adding the column density of the three gas components, we model the total gas distribution at galactocentric radii between 5 and 13 kpc as

$$\Sigma_{\text{gas}}(R) \approx 1.5 \exp\left(\frac{R_{\odot} - R}{2 \text{ kpc}}\right) + 7 M_{\odot} \text{ pc}^{-2}. \quad (9)$$

Then, the product of the gas and the total surface mass densities can be approximated by (see Figure 1)

$$\begin{aligned} \Sigma_{\text{gas}}\Sigma_{\text{tot}} &= \left[1.5 \exp\left(\frac{R_{\odot} - R}{2 \text{ kpc}}\right) + 7 \right] \left[68 \exp\left(\frac{R_{\odot} - R}{2.5 \text{ kpc}}\right) \right] M_{\odot}^2 \text{ pc}^{-4} \\ &\approx 620 \exp\left(\frac{R_{\odot} - R}{2 \text{ kpc}}\right) M_{\odot}^2 \text{ pc}^{-4}, \end{aligned} \quad (10)$$

resulting in a radial distribution of the midplane ISM pressure with the same radial scale length as that of the molecular gas,

$$P_{\text{ISM}}(R) = \frac{\pi G}{2} \Sigma_{\text{gas}}\Sigma_{\text{tot}} \approx P_{\odot} \exp\left(\frac{R_{\odot} - R}{2 \text{ kpc}}\right), \quad (11)$$

therefore, leading to a pressure- H_2 relation in MW within 5 and 13 kpc,

$$\frac{P_{\text{ISM}}}{\Sigma_{\text{H}_2}} \sim \text{constant} \approx \frac{P_{\odot}}{\Sigma_{\text{H}_2}(R_{\odot})}. \quad (12)$$

Since Σ_{HI} is about constant, the ratio $\Sigma_{\text{H}_2}/\Sigma_{\text{HI}}$ is also proportional to P_{ISM} , and is equivalent to the almost linear relationship between the molecular-to-atomic-mass ratio and the system pressure $\Sigma_{\text{H}_2}/\Sigma_{\text{HI}} \propto P_{\text{ISM}}^{0.92}$, found by Blitz & Rosolowsky (2006) for the MW and nearby galaxies.

Another interesting implication of Eq. (12) arises when using $\Sigma_{\text{H}_2}(R_{\odot}) \approx 1.5 \times 10^6 M_{\odot} \text{ kpc}^{-2}$, and the depletion time of the well-defined Kennicutt-Schmidt relation for H_2 found by Bigiel et al. (2008), $\Sigma_{\text{SFR}}/\Sigma_{\text{H}_2} = (7 \pm 3) \times 10^{-10} \text{ yr}^{-1}$:

$$\begin{aligned} \Sigma_{\text{SFR}}(R) &\sim 10^{-9} \frac{P_{\text{ISM}}}{P_{\odot}} \Sigma_{\text{H}_2}(R_{\odot}) M_{\odot} \text{ yr}^{-1} \text{ kpc}^{-2} \\ &\approx 1.5 \times 10^{-3} \left(\frac{P_{\text{ISM}}}{P_{\odot}} \right) M_{\odot} \text{ yr}^{-1} \text{ kpc}^{-2}, \end{aligned} \quad (13)$$

which is also consistent with the slope near unity ($\alpha = 0.92$) obtained by Blitz & Rosolowsky (2006)¹. This relationship represents a lower limit to the rate that is derived from the basic principles and local molecular cloud data discussed in Section 4.2.

In addition, note that the radial distributions of Σ_{tot} and Σ_{gas} become about equal at a Galactic radius close to 13 kpc, where the midplane pressure drops to about a 10th of its solar circle value. This location is almost coincident with the truncation radius of the old stellar disk, 12 kpc (Freudenreich 1998), and the location where the atomic gas density begins to decrease exponentially at 13 kpc (Kalberla & Dedes 2008). Also, the vertical scale height of the gaseous disk flares up close to this distance, as shown in the compilation of Bacchini et al. (2019), and one would expect that the vertical distribution of the gas may change from an exponential function into

¹ The value at the solar circle, $1.6 \times 10^{-3} M_{\odot} \text{ yr}^{-1} \text{ kpc}^{-2}$, is similar to that derived by Lee et al. (2016), and a factor of ~ 2 smaller compared to the normalization derived by Sun et al. (2023). This difference is within the dispersion derived in this relation of $\sigma = 0.33$ dex (Sun et al. 2023), and gives values within those derived from observations; see Section 4.2.

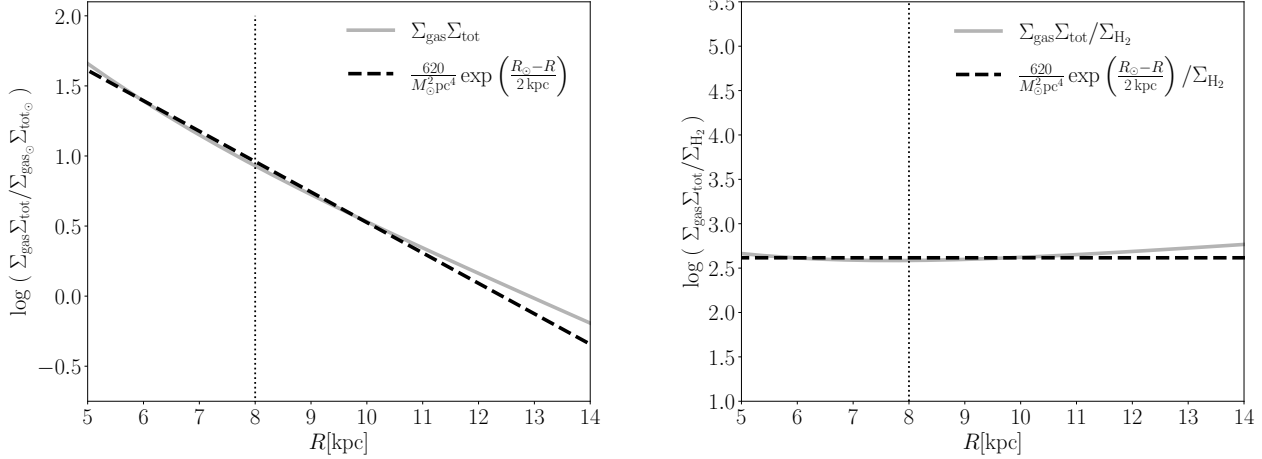


Figure 1. Left Panel: The product of surface gas mass density and total mass surface density (solid line) and the approximate fit (dashed line), as a function of galactocentric radius. **Right Panel:** The product of the surface gas mass density and total mass surface density divided by the molecular surface gas mass density. This is proportional to the pressure-H₂ relation described in the text and shows that $P_{\text{ISM}}/\Sigma_{\text{H}_2}$ is almost constant between 5 and 12 kpc. In both panels, the dotted lines shows the location of our assumed solar circle, $R_\odot = 8$ kpc.

an isothermal self-gravitating gaseous disk with a sech^2 distribution somewhere close to this location (e.g., Spitzer 1942).

Finally, with eqs. (6) and (11), the resulting average volume density of diffuse pressure-bounded clouds in the disk can be written as:

$$n_{\text{cl}}(R) = \frac{\pi G \Sigma_{\text{gas}} \Sigma_{\text{tot}}}{12kT_{\text{eff}}} \approx 33 \left(\frac{P_{\text{ISM}}}{P_\odot} \right) T_{100}^{-1} \text{ cm}^{-3}, \quad (14)$$

where T_{100} is the temperature of the cloud gas in units of 100 K. The resulting values of n_{cl} are a decreasing function of the galactocentric distance giving, for $T_{100} \sim 1$, a range of average densities between $\sim 200 \text{ cm}^{-3}$ at 5 kpc and $\sim 10 \text{ cm}^{-3}$ at 10 kpc, consistent with those observed for diffuse clouds (see Snow & McCall 2006; Goldsmith 2013; Neufeld et al. 2024) and those modeled for CNM by Wolfire et al. (2003).

Next, we discuss the conditions under which these CNM clouds, embedded within the warm neutral medium (see Kalberla & Haud 2018; Park et al. 2023), can be transformed into molecular clouds and the rate at which this transformation occurs.

3 MOLECULAR CLOUDS

The formation of molecular clouds (and eventually stars) can be viewed as a fragmentation process (Franco & Cox 1986) in which the first step occurs when the central region of an initially cold atomic cloud is shielded from the external UV radiation field at wavelengths close to $\lambda \sim 10^{-5}$ cm. This shuts down its primary heat source, prevents the dissociation of H₂, and causes the eventual formation of a cooler and denser molecular cloud. As is already known, the external layers of molecular clouds are atomic transition regions, photodissociated regions (PDR), whose column densities protect the interior from the dissociating photons. Interstellar dust grains play three important roles in the fragmentation process. First, molecular hydrogen is formed on the grain surface lattice, second, small grains maintain the temperature of the gas through photoelectric heating, and third, the opacity of the small dust at the wavelengths of the dissociating Lyman and Werner bands near $\lambda \sim 10^{-5}$ cm reduces the photodissociation rate, protecting the newly formed H₂. Here we

explore the role of Galactic parameters in controlling the formation process of the resulting molecular clouds.

3.1 Far ultraviolet dust extinction cross section:

Following the simplified scheme of Franco & Cox (1986, FC86), the average mass density of dust grains in the ambient ISM, $\langle \rho_{\text{ISM,d}} \rangle$, is

$$\langle \rho_{\text{ISM,d}} \rangle \approx n_{\text{d}} \rho_{\text{d}} V_{\text{d}}, \quad (15)$$

where n_{d} is the number density of interstellar grains, ρ_{d} is the internal mass density of a dust grain, and $V_{\text{d}} = 4\pi a^3/3$ is the volume of solid and homogeneous spherical grains with an average radius a (for porous or multilayer grains one can use an equivalent size parameter, see Voshchinnikov et al. 2006). This average dust mass density in the ISM can be written in terms of metallicity Z , the dust-to-metal mass ratio f_d (the fraction of heavy elements locked in the dust grains) and the mass density of the gas μn_T (where $\mu = 2.27 \times 10^{-24}$ g is the mass per proton including He and $n_T = n_H + 2n_{H_2}$ is the average number density of protons) as,

$$\langle \rho_{\text{ISM,d}} \rangle \approx Z f_d \mu n_T. \quad (16)$$

Then, the far-ultraviolet (FUV) extinction cross section per H atom can be written as

$$\sigma_{\text{UV}} \sim \pi a_{\text{UV}}^2 Q_{\text{ext}} \frac{n_{\text{d}}}{n_T} \approx \frac{3 Q_{\text{ext}} Z f_d \mu}{4 a_{\text{UV}} \rho_{\text{d}}}, \quad (17)$$

where $Q_{\text{ext}} \sim 2.4$ is the extinction efficiency for compact, porous, or multilayer grains of effective size $a_{\text{UV}} \sim \lambda \sim 10^{-5}$ cm (e.g., Voshchinnikov et al. 2006), and we take $\rho_{\text{d}} \sim 2.5 \text{ gr cm}^{-3}$ as the average mass density within a grain (the internal densities of interplanetary dust grains range from 0.3 to 6.2 g cm⁻³; Love et al. 1994). With these values, the FUV cross section is

$$\sigma_{\text{UV}} \approx 1.6 \times 10^{-19} f_d Z \text{ cm}^2. \quad (18)$$

This linear dependence on Z was first proposed by FC86, and was later independently adopted by several authors in the construction of PDR models (e.g., Wolfire et al. 2008; Krumholz et al. 2008, 2009; McKee & Krumholz 2010; Sternberg et al. 2014; Maillard et al.

2021). However, a review of the observational restrictions imposed on the dependence on Z and f_d , both of which are related to the dust-to-gas mass ratio, D/G , indicates that the dependence is not linear for metallicities $\leq (0.1 - 0.2)Z_\odot$, where it becomes much steeper (Rémy-Ruyer et al. 2014; De Vis et al. 2019; Péroux & Howk 2020).

3.1.1 The dust-to-gas mass ratio, D/G , in nearby galaxies:

The relationship of σ_{UV} with metallicity is linear, provided that the dust-to-gas mass ratio D/G is also linear with Z . Several nearby galaxies show radial trends of D/G that seem to be correlated with their metallicity gradients (e.g., Issa et al. 1990; Boissier et al. 2004; Muñoz-Mateos et al. 2009; Mattsson & Andersen 2012; Vilchez et al. 2019), and in a sample of 126 nearby galaxies, Rémy-Ruyer et al. (2014) derived a linear growth at metallicities higher than $12 + \log(O/H) \sim 8$, but the relationship changed to a cubic dependence for lower values. This break in the Z dependence occurs at about $0.2 Z_\odot$, where $Z_\odot \approx 1.96 \times 10^{-2}$ is the solar metallicity (von Steiger & Zurbuchen 2016), and $12 + \log(O/H)_\odot \sim 8.69$ is the value of the oxygen abundance in the solar circle (Asplund et al. 2009).

The nonlinear dependency at low metallicities was confirmed by De Vis et al. (2019), who derived the values of D/G as a function of Z for some 500 galaxies from DustPedia (Clark et al. 2018) and other catalogs. They concluded that their data, which cover the same range of values of Rémy-Ruyer et al. (2014) but have a larger scatter, can be best fitted by a single power law with an exponent of 2.45.

More recently, Péroux & Howk (2020) and Roman-Duval et al. (2022b) made compilations of these and other studies, showing that the integrated values of the MW and Magellanic Clouds follow an almost linear dependence, with an integrated value for the MW of $(D/G)_{\text{MW}} \sim 8 \times 10^{-3}$. In addition, Clark et al. (2023)² and Hamanowicz et al. (2024) obtained integrated values for other members of the Local Group (M31, M33, IC1613 and Sextans A), which also lie in the same almost linear track of the MW and Magellanic Clouds. The linear trend is also consistent with the results found by Draine et al. (2007) and with those found by Wiseman et al. (2017) for galaxies with a high redshift. In addition, it should be noted that damped Lyman- α absorbers also display an intriguing linear relationship with metallicity.³

Dust evolution models in disk galaxies can reproduce the main features and radial trends of D/G versus Z observed in nearby galaxies and indicate that dust formation can also occur in the ISM (e.g., Mattsson & Andersen 2012; Feldmann 2015; Zhukovska et al. 2016; Hou et al. 2019; Aoyama et al. 2020). Together, these theoretical and observational results indicate that the linear dependence can be used for metallicities above $\sim 0.2 Z_\odot$, but the relationship is much steeper, approximately cubic, below this value.

² Clark et al. (2023) found a correlation between D/G and Σ_{HI} for M31, M33 and the Magellanic Clouds, but given their flat (or non-existent) metallicity gradient, this is not related with Z and may indicate dust growth in regions with high gas densities. The same argument applies to the dependence of elemental depletions on gas density fluctuations in the MW and Magellanic Clouds (e.g., Roman-Duval et al. 2022a)

³ De Cia et al. (2016) and De Cia et al. (2018) found an almost linear relationship of D/G with Z in damped Lyman- α absorbers covering two orders of magnitude in Z that can be extended to those found in MW clouds. The trend and data are less scattered than those found in nearby galaxies, and a large fraction of their metallicity, probably most of it, seems to be locked in dust grains.

3.1.2 The dust-to-metal mass ratio, f_d , in nearby galaxies:

The equilibrium values of the dust-to-metal mass ratio in the ISM, defined as $f_d = D/M = (D/G)/Z$, depend on the formation, growth, and destruction mechanisms of the grains that operate in the ISM. Thus, for metallicities above $0.2 Z_\odot$, where D/G is linear with Z , it is expected that f_d should reach a constant value after the dust lifecycle reaches equilibrium within a given galactic system.

Data compilation of 15 nearby galaxies by Mattsson & Andersen (2012) display radial gradients in both D/G and f_d , but the trends in f_d are much flatter and in some cases are almost constant. These shallow trends are approximately reproduced by numerical models of chemical enrichment and dust evolution in gaseous disks of late-type galaxies (e.g., Mattsson & Andersen 2012; Aoyama et al. 2020), and these and other models indicate that as the amount of dust-forming elements decreases by depletion in the gas phase, dust growth slows and f_d tends to a constant value (see Chiang et al. 2021 and references therein). Interestingly, the constancy of f_d has been found even in metal-poor systems with $Z \sim 10^{-2} Z_\odot$ by Zafar & Watson (2013).

Chiang et al. (2021) performed a detailed study of the dust-to-metal ratio in five nearby galaxies and found that they are about constant within each galaxy, with equilibrium values ranging from 0.4 to 0.58. Their data have less scatter compared to other similar studies (see Figures 5 and 6 of Chiang et al. 2021), and are also consistent with a linear dependence of D/G on Z at metallicities greater than $0.2 Z_\odot$. For the metallicity in the solar neighborhood, their results and the linear fit of Rémy-Ruyer et al. (2014) give an average equilibrium value close to $f_d \sim 0.6$. Thus, using Eqs. (17) and (18) with $f_d \sim 0.6$, we recover the cross-sectional value of FC86,

$$\sigma_{\text{UV}} \approx 1.9 \times 10^{-21} (Z/Z_\odot) \text{ cm}^2. \quad (19)$$

But its validity is now limited to metallicities greater than $\sim 0.2 Z_\odot$ and the value in the solar circle is similar to those derived from observations in the diffuse medium with an optical extinction of $A_v/E(B-V) \approx 3.1$, and to those used in PDR models (e.g., Bohlin et al. 1978; Draine & Bertoldi 1996; Röllig et al. 2007; Krumholz et al. 2008; Röllig et al. 2013; Maillard et al. 2021; Shull et al. 2021).

3.1.3 The H_2 formation rate as a function of P_{ISM} :

One of the first molecules to be formed in a nascent molecular cloud is H_2 , less abundant molecules are formed later. Its formation rate on the surface of dust grains is $n_{\text{HI}} n_T R_f$, so the formation rate per hydrogen atom and unit time is

$$F = n_T R_f, \quad (20)$$

where n_{HI} is the abundance of atomic hydrogen, $n_T = n_{\text{HI}} + 2n_{H_2}$ is, as above, the average total abundance of protons, and the rate coefficient for the formation of H_2 on grains is (Hollenbach & McKee 1979)

$$R_f = \frac{n_d \sigma_d}{n_T} \langle S_v \rangle f_a, \quad (21)$$

where n_d is the volumetric density of dust grains in the cloud, σ_d is the grain cross section for collisions with atomic hydrogen, f_a is the fraction of H atoms that stick to the grain to form H_2 , and $\langle S_v \rangle \approx 7 \times 10^4 T_{100}^{1/2} \text{ cm s}^{-1}$ is the average velocity of the incoming H atoms. For CNM clouds, which have low T and the expected value of f_a tends to 1, the approximation of Hollenbach & McKee (1979) and the results of Jura (1975a) from UV observations give a rate coefficient of $R_f \sim 3 \times 10^{-17} T_{100}^{1/2} \text{ cm}^3 \text{ s}^{-1}$.

For pressure bounded clouds, n_T is proportional to P_{ISM}/T_{100}

(eq. 14), and the formation rate per hydrogen atom (Eq. 20) can be approximated by

$$F \sim 10^{-15} \left(\frac{P_{\text{ISM}}}{P_{\odot}} \right) T_{100}^{-1/2} \text{ s}^{-1} \quad (22)$$

$$\approx 3.16 \times 10^{-8} \left(\frac{P_{\text{ISM}}}{P_{\odot}} \right) T_{100}^{-1/2} \text{ yr}^{-1}.$$

Thus, the transformation of HI into H₂ in the inner parts of a diffuse cloud is directly controlled by ambient pressure. In addition, given that dust opacity depends on Z , the net result is that the formation of molecular clouds depends on both P_{ISM} and Z and the process is faster and more efficient in the inner regions of galaxies, where both pressure and metallicity are higher.

3.2 Atomic to molecular transition regions

Details of the PDR region that separates the diffuse medium from the molecular gas have been explored for the last five decades with a number of different models and methods (e.g., Hollenbach & Salpeter 1971; Glassgold & Langer 1974; Jura 1975b,c; Federman et al. 1979; de Jong et al. 1980; Tielens & Hollenbach 1985; Elmegreen 1989; Abgrall et al. 1992; Draine & Bertoldi 1996; Browning et al. 2003; Röllig et al. 2007; Krumholz et al. 2008; McKee & Krumholz 2010; Sternberg et al. 2014; Gong et al. 2017; Maillard et al. 2021). The impinging FUV radiation field at $\lambda \geq 916 \text{ \AA}$ is usually expressed in units of the local interstellar field described by Habing (1968), $4 \times 10^{-17} \text{ erg cm}^{-3} \text{ \AA}^{-1}$, or in terms of the updated value derived by Draine (1978), which is 1.71 higher. As these photons enter a certain distance from the external edge of the cloud, their intensity decreases due to the opacity of the dust, and the corresponding photodissociation rate in unidirectional plane-parallel approximations drops as $\exp(-\tau_d)$, where $\tau_d = \int \sigma_{\text{UV}} n_T dx$ is the optical depth. As molecules begin to form, they absorb FUV photons and increase opacity.

For isotropically illuminated models, the attenuation of the radiation field at a given point from the external cloud boundary is smaller than in unidirectional models because the incoming photon flux comes from different directions, and this is further complicated when dust scattering is included (e.g., Flannery et al. 1980; Röllig et al. 2007). Given that molecular clouds, either individual or in cloud complexes, have irregular or filamentary shapes without preferred geometries, unidirectional and plane-parallel configurations have been used as a reasonable approach to the problem (see, e. g., Gong et al. 2017).

With this approach, FC86 proposed that a proxy for the column density to protect the center of the cloud from dissociating radiation in the solar neighborhood can be approximated by the condition of $\tau_d \sim 1$,

$$N_d \approx \sigma_{\text{UV}}^{-1} \approx 5 \times 10^{20} \left(\frac{Z_{\odot}}{Z} \right) \text{ cm}^{-2}. \quad (23)$$

Or, equivalently, diffuse clouds with a radius larger than

$$r_{\tau} = \frac{N_d}{n_{\text{cl}}} \approx 3 \left(\frac{Z_{\odot}}{Z} \right) \left(\frac{P_{\odot}}{P_{\text{ISM}}} \right) T_{100} \text{ pc}, \quad (24)$$

become molecular at their centers. These threshold values are more than satisfied by the amount of mass gathered in convergent gas flows, instabilities, or shocks in spiral arms (e.g., Jog & Solomon 1984; Elmegreen 1987; Hartmann et al. 2001; Kim & Ostriker 2002; Franco et al. 2002; Schaye 2004; Zamora-Avilés et al. 2019b). As the amount of molecules accumulates in its interior, the original cold

diffuse cloud readjusts its original structure to a centrally condensed configuration: becoming denser and cooler at the core, while remaining atomic and warmer at the peripheral layers, but in pressure equilibrium with the ambient medium. Also, given that the central cloud temperatures are lower, the corresponding velocity dispersions should increase toward the center of the cloud (see Ballesteros-Paredes et al. 2011).

This simple proxy provides remarkable results. Observations in the ultraviolet indicate that the threshold for molecular cloud formation in the MW is achieved when the ratio of molecular to total column density is $2N_{\text{H}_2}/N_{\text{H}} \approx 0.1$, where $N_{\text{H}} = N(\text{H}) + 2N(\text{H}_2)$, resulting in a transition region with a total column density of gas of approximately $\sim 5 \times 10^{20} \text{ cm}^{-2}$ (e.g., Savage et al. 1977; Bohlin et al. 1978; Federman et al. 1979; Shull et al. 2021; Park et al. 2023), similar to Eq. (23) and equivalent to a mass layer of $\sim 5 M_{\odot} \text{ pc}^{-2}$. The proxy is also consistent with the threshold of the HI-H₂ transition region derived from FUV observations in Magellanic Clouds (Tumlinson et al. 2002; Browning et al. 2003; Shull et al. 2021), where the average integrated metallicity values are $Z_{\text{LMC}} \sim 0.5 Z_{\odot}$ and $Z_{\text{SMC}} \sim 0.2 Z_{\odot}$ (e.g., Roman-Duval et al. 2022a) and is also consistent with the FUV observations of H₂ in starburst galaxies (Hoopes et al. 2004).

On the other hand, as noticed by Martin & Kennicutt (2001, see also Wong & Blitz 2002) in a sample of 32 galaxies, disks become dominated by HI gas when the gas density drops below $5 - 10 M_{\odot} \text{ pc}^{-2}$. Later, Bigiel et al. (2008) showed that for 18 nearby spirals the transition from atomic to molecular gas can occur around $\sim 10 M_{\odot} \text{ pc}^{-2}$ corresponding to a column density of $\sim 10^{21} \text{ cm}^{-2}$ (see their Figure 8). This value coincides with the proxy along the entire cloud, namely $2N_d$,

$$2N_d = 2 \sigma_{\text{UV}}^{-1} \approx 10^{21} \left(\frac{Z_{\odot}}{Z} \right) \text{ cm}^{-2}, \quad 2\Sigma_d \approx 10 \left(\frac{Z_{\odot}}{Z} \right) M_{\odot} \text{ pc}^{-2}, \quad (25)$$

and to that required for the appearance of local dynamical instabilities that lead to a transition to cold ISM phases, as derived by Schaye (2004). Therefore, despite its simplicity, the $\tau_d \sim 1$ condition provides a reasonable approximation to the observed transition values in the Local Group and nearby spirals.

One may ask how such a simple criterion compares with the results of elaborate PDR models. Shull et al. (2021) made an analytical match of their observational FUV results for the transition region using detailed stationary PDR models from Draine & Bertoldi (1996) (these include dust opacity, self-shielding of thousands of H₂ lines, and the effects of line overlap). They found that their observations are explained by an optical depth of dust of $\tau_d = 1.013$. To complement this result, we derive the corresponding equilibrium volume density of H₂ at the location of the transition point using the formation rate described above and the approximation to the photodissociation rate given by Draine & Bertoldi (1996),

$$G_{\text{diss}} \approx f_{\text{shield}} \exp(-\tau_d) G_d, \quad (26)$$

where $f_{\text{shield}} = 3.16 \times 10^{10} N(\text{H}_2)^{-3/4}$ is the shielding function and G_d is the photodissociation rate at the external edge of the cloud. For the solar neighborhood, the ambient FUV radiation field derived by Habing (1968) gives a photodissociation rate at the external edge of the cloud, $G_{\odot} \sim 6 \times 10^{-11} \text{ s}^{-1}$ (Federman et al. 1979) and, as usual, we write $G_d = \chi G_{\odot}$ to allow for different intensities of the FUV field (the updated value of Draine (1978) corresponds to $\chi = 1.71$).

With these numbers, the equilibrium molecular-to-atomic ratio at

$\tau_d \sim 1$ is

$$\frac{n_{H_2}}{n_{HI}} = \frac{n_T R_f}{f_{\text{shield}} \exp(-\tau_d) G_d} \approx 0.3 \left(\frac{\chi}{1.71} \right)^{-1} \left(\frac{P_{\text{ISM}}}{P_{\odot}} \right) T_{100}^{-1/2}, \quad (27)$$

and the resulting fraction of H_2 at the point of transition is

$$\frac{n_{H_2}}{n_T} \sim 0.2 \left(\frac{\chi}{1.71} \right)^{-1} \left(\frac{P_{\text{ISM}}}{P_{\odot}} \right) T_{100}^{-1/2}. \quad (28)$$

Therefore, as expected, most of the gas in the HI- H_2 transition layer is atomic and, aside from its dependence on the FUV radiation field, the fractional abundance of H_2 in the cloud interior is regulated by the pressure of the system.

Several observational results, ranging from radio waves to the FUV in the MW and in nearby spirals and irregulars, indicate that there is a coincidence in the threshold to the existence of molecular clouds and the formation of stars, occurring at gas column densities in the range $\sim 5 - 15 M_{\odot} \text{ pc}^{-2}$ (e.g., Skillman 1987; Kennicutt 1979; Martin & Kennicutt 2001; Wong & Blitz 2002; Bigiel et al. 2008). However, we note that, despite similarities in numerical values, they refer to fundamentally different issues. The transition region in the FUV refers to the column density of the mainly atomic hydrogen layers that surround any molecular cloud, Σ_d , while the threshold for star formation refers to the surface density of the molecular hydrogen mass, Σ_{H_2} inside the clouds.

3.3 Radial threshold conditions

Using the radial gradient of O/H obtained by Arellano-Córdova et al. (2021) as the metallicity tracer for the MW, $12 + \log(O/H) \approx 8.84 - 0.042 R$, the radial variation between 5 and 13 kpc can be approximated by

$$Z \approx Z_{\odot} \exp \left(\frac{R_{\odot} - R}{10 \text{ kpc}} \right). \quad (29)$$

Note that our selected (O/H) value for the solar circle in §3.1.1 is smaller than the one used by Arellano-Córdova et al. (2021) but is in better agreement with their actual fit at 8 kpc. The resulting threshold mass column density variation along the disk of the MW is then (see Eq. 25),

$$\Sigma_d \approx 5 \exp \left(\frac{R - R_{\odot}}{10 \text{ kpc}} \right) M_{\odot} \text{ pc}^{-2}. \quad (30)$$

For locations close to the molecular ring at 4 kpc, the corresponding pressure is about six times higher, and the metallicity is about 1.5 times higher than those at the solar circle, and cold clouds with mass surface densities as small as $3 M_{\odot} \text{ pc}^{-2}$ and radii as small as ~ 0.3 pc fulfill the requirement to become molecular.

Given that the population of molecular clouds is controlled by metallicity and system pressure, the obvious and well-known result is that most of the molecular mass should be concentrated in the inner parts of the gaseous disk. Another consequence of the larger pressure values within the solar circle, which is also obvious, is that the average densities of individual molecular clouds should be higher, in accordance with those derived for individual clouds in the compilation of Miville-Deschénes et al. (2017a).

3.4 Pressure-regulated formation of molecular gas along the disk of the MW

Recent emission and absorption studies of atomic hydrogen show that, in addition to the already known cold and warm stable phases,

the third and unstable "lukewarm" phase is also prevalent in the disk of the MW (Kalberla & Haud 2018; Park et al. 2023; Gupta et al. 2025). The relative fraction of these three phases is somewhat similar and, assuming that the actual precursor of molecular clouds is the CNM phase, only about a third of $\Sigma_{HI} \approx 5 M_{\odot} \text{ pc}^{-2}$ (see Section 2.2) is available to form molecular clouds. The resulting rate of molecular gas formation per unit surface in the MW disk, $\dot{\Sigma}_{\text{mol}}^+$, is simply given by the product of $\Sigma_{HI}/3 \approx 1.7 M_{\odot} \text{ pc}^{-2}$ with the formation rate of H_2 per hydrogen atom, Eq. (22),

$$\begin{aligned} \dot{\Sigma}_{\text{mol}}^+ &= \frac{\Sigma_{HI} F}{3} \sim 1.7 \times 10^{-9} \left(\frac{P_{\text{ISM}}}{P_{\odot}} \right) T_{100}^{-1/2} M_{\odot} \text{ kpc}^{-2} \text{ s}^{-1} \\ &\approx 5 \times 10^{-2} \exp \left(\frac{R_{\odot} - R}{2 \text{ kpc}} \right) T_{100}^{-1/2} M_{\odot} \text{ kpc}^{-2} \text{ yr}^{-1}. \end{aligned} \quad (31)$$

This H_2 mass formation rate can be termed pressure-regulated and assuming that the cycling of the gas components of the disk is in dynamical equilibrium, it should be equal to the rate of destruction of the molecular gas per unit surface, $\dot{\Sigma}_{\text{mol}}^-$.

The destruction rate is the sum of the transformation of the molecular mass into stars and the evaporation of the parental clouds due to the injection of energy from newly formed stars. Thus, the cycling between atomic and molecular gases owing to stellar feedback in equilibrium is also regulated by pressure, which supports the self-regulated model of Ostriker et al. (2010). In the solar circle, then, the rate of molecular cloud destruction should be about $\sim 5 \times 10^{-2} M_{\odot} \text{ kpc}^{-2} \text{ yr}^{-1}$, and its implications are discussed in the next section. Note that in the hypothetical case where no stars are formed, $\dot{\Sigma}_{\text{mol}}^- = 0$, the molecularization of the disk occurs inside-out and on a time scale of about $\Sigma_{HI}/\dot{\Sigma}_{\text{mol}}^+ \sim 10^8 (P_{\odot}/P_{\text{ISM}}) T_{100}^{1/2} \text{ yr}$.

4 SELF GRAVITATING CLOUDS AND STAR FORMATION

The onset of self-gravity is achieved when the gravitational energy of an initially pressure-confined cloud is similar to its internal energy $GM_{\text{cl}}^2/R_{\text{cl}} \sim P_{\text{ISM}} V_{\text{cl}}$, and the corresponding threshold mass surface density across the cloud is

$$\Sigma_{\text{sg}} \approx \left(\frac{4P_{\text{ISM}}}{\eta G} \right)^{1/2}, \quad (32)$$

where $V_{\text{cl}} = \eta R_{\text{cl}}^3$ is the volume of the cloud, and the geometric factor for uniform spherical clouds is $\eta_s = 4\pi/3$. Note that this surface mass density criterion is equivalent to the one derived from the Jeans length criterion⁴. For the solar circle, the threshold value is

$$\Sigma_{\text{sg},\odot} \sim 30 \left(\frac{\eta_s}{\eta} \right)^{1/2} M_{\odot} \text{ pc}^{-2}, \quad (33)$$

and its radial distribution along the disk is

$$\Sigma_{\text{sg}} = \Sigma_{\text{sg},\odot} \left(\frac{P_{\text{ISM}}}{P_{\odot}} \right)^{1/2} \sim 30 \left(\frac{\eta_s}{\eta} \right)^{1/2} \exp \left(\frac{R_{\odot} - R}{4 \text{ kpc}} \right) M_{\odot} \text{ pc}^{-2}. \quad (34)$$

Thus, the formation of self-gravitating clouds also depends on the pressure of the system, and the required surface mass density for the transformation of a molecular cloud into a self-gravitating entity

⁴ Except for a factor close to unity, this result is equal to the product of twice the Jeans length for spherical clouds $L_J = [15kT/(4\pi\mu G\rho_{\text{cl}})]^{1/2}$ and the average mass density of our pressure-bounded clouds $\rho_{\text{cl}} = \mu P_{\text{ISM}}/(6kT)$, $2L_J\rho_{\text{cl}} = \Sigma_J = [20P_{\text{ISM}}/(8\pi G)]^{1/2}$.

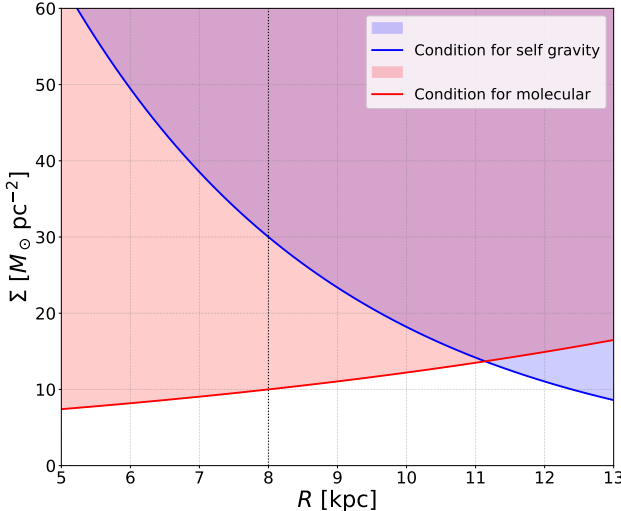


Figure 2. The threshold mass surface density across the whole cloud to become molecular, $2\Sigma_d$ (red line), and the threshold condition to become self-gravitating, Σ_{sg} (blue line). Clouds with gas mass surface densities above the red line are molecular (shaded in pink), while those above the blue line are self-gravitating (shaded in blue).

can be collected via gravitational or magnetic instabilities or by the convergence of large-scale streams of gas (Ballesteros-Paredes et al. 1999a,b; Hartmann et al. 2001; Franco et al. 2002; Lee et al. 2004; Vázquez-Semadeni et al. 2007; Heitsch & Hartmann 2008). At some moment in the assembly process, the gravitational energy becomes greater than the sum of the internal energies of the cloud, and its interior decouples from the pressure of the system.

Figure 2 shows the molecular and self-gravity threshold criteria, and they become equal at a galactocentric distance of about ~ 11 kpc. This distance marks the location inside which the star-forming clouds follow a two-step evolution. First, they become molecular, and then, after contracting or gathering mass from the external medium, their column density increases, and they become self-gravitating, starting a track towards the formation of stars, typically in a hierarchically and nonmonolithic mode (e.g., Ballesteros-Paredes et al. 2011; Vázquez-Semadeni et al. 2019). The figure also shows, as noted by Evans et al. (2021b), that even when molecular clouds in the inner galaxy have larger surface mass densities, they are not necessarily self-gravitating.

For locations outside 11 kpc, the decrease in both pressure and metallicity results in less dense and less opaque clouds. As a consequence, the population of molecular clouds should drop, but the existing ones first became self-gravitating, when they reached total gas column densities of about $12 M_\odot \text{ pc}^{-2}$, and then became molecular after reaching the opacity criterion. In these external regions, then, the evolution of clouds is different, and the star formation process can also occur in small molecular clouds and even in mainly atomic clouds. This is in line with the results of the high-resolution survey of molecular clumps in the outer MW by Urquhart et al. (2025), where the fraction of low-mass star-forming clumps is higher than in the inner MW. Also, this possibility may be at work in the formation of intergalactic HII regions (see Ryan-Weber et al. 2004).

In a study with more than 8100 molecular clouds in the Milky Way, Miville-Deschénes et al. (2017b) obtained the physical properties and radial trends of individual clouds located as far as 20 kpc from the Galactic center. They found that the densities (both volumetric and

per unit area), as well as the velocity dispersions, are substantially larger in the inner galaxy than in the outer parts, as expected from the results of the previous section.

The median of mass surface values for individual clouds located between 6 and 10 kpc follows the trend of interstellar pressure, and coincidentally scales with one-half of the value of the threshold for self-gravity at the solar circle, $\Sigma_{sg,\odot}/2$ (see their Figure 9),

$$\Sigma_{\text{median}} \sim 0.5 \Sigma_{sg,\odot} \left(\frac{P_{\text{ISM}}}{P_\odot} \right) \approx 15 \exp \left(\frac{R_\odot - R}{2 \text{ kpc}} \right) M_\odot \text{ pc}^{-2}. \quad (35)$$

This may be another indication that the physical properties of the molecular cloud population are controlled by the pressure of the system, and, given that the median value implies that half of the clouds are below such a value, a good fraction of the clouds in the compilation of Miville-Deschénes et al. (2017a) are not self-gravitating.

In order to compare this result with our expected total surface mass density of H_2 at the threshold of self-gravity, we have to subtract the contribution of the atomic layers that surround the central molecular gas. Then, the total H_2 surface mass density across a cloud at the threshold of self-gravity is $\Sigma_{t,\text{mol}} = \Sigma_{sg} - 2\Sigma_d$,

$$\Sigma_{t,\text{mol}} \approx \left[30 \left(\frac{\eta_s}{\eta} \right)^{1/2} \exp \left(\frac{R_\odot - R}{4 \text{ kpc}} \right) - 10 \exp \left(\frac{R - R_\odot}{10 \text{ kpc}} \right) \right] M_\odot \text{ pc}^{-2}. \quad (36)$$

Figure 3 compares Eq. (36) with the median values of the compilation of Miville-Deschénes et al. (2017a). It shows that molecular clouds inside 6 kpc and outside 10 kpc tend to be self-gravitating but, as expected, a good fraction of molecular clouds between 6 and 10 kpc are not gravitationally bound. This is also in line with the fact that a large number of the cloud population display virial parameters well above the value expected for gravitationally bound systems, as pointed out by Evans et al. (2021b).

Also note that our criterion in the solar neighborhood corresponds to about $\Sigma_{t,\text{mol}}(R_\odot) \sim 20 (\eta_s/\eta)^{1/2} M_\odot \text{ pc}^{-2}$. For $(\eta_s/\eta)^{1/2} = 1$, it is higher than the range of observed threshold molecular column densities for star formation, $\sim 5 - 15 M_\odot \text{ pc}^{-2}$ (e.g., Skillman 1987; Martin & Kennicutt 2001; Wong & Blitz 2002; Bigiel et al. 2008), but the observational values can be matched if $(\eta_s/\eta)^{1/2} \sim (0.3 - 0.7)$, indicating that clouds are possibly filamentary.

4.1 Arm-interarm pressure differences

Concerning the role played by spiral arms⁵, there are numerous studies exploring their role in star formation, including large-scale magnetic instabilities, gravitational fragmentation within the arms, and the formation of dust lanes due to the arm-interarm interaction (e.g., Franco et al. 2002; Kim et al. 2002; Bonnell et al. 2013; Renaud et al. 2013; Khoperskov et al. 2013; Elmegreen & Elmegreen 2019, and references therein). For our purposes, it is sufficient to say that the pressure inside the arm increases because the total mass and gas surface densities are higher than in the inter-arm regions. For example, in the case of arms located at 4.5 and 6.5 kpc in the MW, Marasco et al. (2017) found that the surface mass densities of both HI and H_2 are factors approximately 1.5 to 2 above the average

⁵ See Khoperskov et al. (2013) and Khoperskov et al. (2016) for the formation of molecules and molecular clouds along the arms

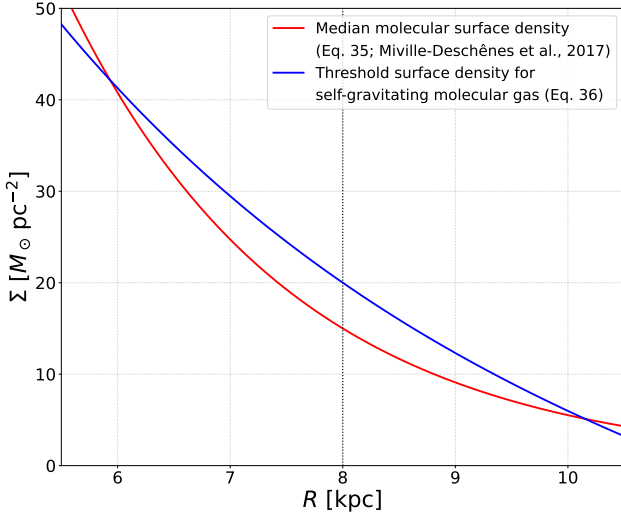


Figure 3. The median mass surface density between 6 and 10 kpc from the compilation of [Miville-Deschénes et al. \(2017b\)](#), as approximated in Eq. (35) (red line). The total H₂ surface mass density threshold condition to become self-gravitating of our model, from Eq. (36) (blue line).

values at these locations, while external galaxies show similar H₂ contrasts ([Querejeta et al. 2024a](#)). The models of [Gómez & Cox \(2004\)](#), [Khoperskov et al. \(2013\)](#) and [Mata-Chávez et al. \(2019\)](#) for spiral arms in normal spirals indicate that the total mass surface density increases by a factor of about two or three. Thus, the product $\Sigma_g \Sigma_{tot}$ within the arms is about a factor of 4 above the interarm regions, and the arm pressure increases by the same factor. This also increases the cloud densities by the same factor, directly increasing the rate at which molecules are formed within the arms and leading to the prevalence of dense molecular clouds along the arms.

Cloud agglomeration and instabilities also result in most giant molecular clouds located inside the arms. In addition, the radiative shock front associated with the passage of the arm compresses even further the already dense molecular clouds and can trigger the rapid formation of stars, making these locations preferential sites for star formation. Our scheme indicates that the surface density contrast of the arm-interarm H₂ gas should be proportional to the pressure contrast. The H₂ surface density data of [Marasco et al. \(2017\)](#), displayed in their Figure 10, show that the arm-interarm surface density contrast is indeed between 3 and 4, close to the one expected from our pressure-regulated scheme.

An additional issue is that the arm shock front in a magnetized medium produces a hydraulic jump, sending gas to high latitudes ([Martos & Cox 1998](#)) and can even induce star formation outside the main gaseous disk ([Martos et al. 1999](#)). The HI data of [Marasco et al. \(2017\)](#) show an increase in the gas scale height (possibly due to the passage of the arms), and this increase is offset by about 1 kpc from the locations of the gas density peaks (see their figures 11, 14 and 15). A recent study with 3D dust maps by [Kormann et al. \(2025\)](#) has discovered large wave-like gas structures in the solar neighborhood. These are kiloparsec-sized atomic superclouds with corrugations locating the gas above and below the midplane. It is unclear whether they are associated or not with the passage of any spiral arm, but they resemble the outcome of the Parker instability in 3D (see [Franco et al. 2002](#)).

4.2 Pressure-regulated star formation per unit area in the disk of the MW

Observational studies show that compared to other spirals, where interstellar pressure values can reach $\log(P_{ISM}/k) \sim 8.5$ (e.g., [Blitz & Rosolowsky 2006](#); [Fisher et al. 2019](#); [Barrera-Ballesteros et al. 2021](#); [Sun et al. 2023](#); [Ellison et al. 2024](#)), the MW disk can be considered a low-pressure system with modest values up to $\log(P_{ISM}/k) \sim 5$. These works also show that the surface density of star formation increases approximately linearly with pressure for $\log(P_{ISM}/k) \leq 5.5$ but the trend becomes shallower at higher pressures (e.g., [Fisher et al. 2019](#); [Barrera-Ballesteros et al. 2021](#); [Ellison et al. 2024](#)). This linear relation with P_{ISM} has been deduced by models of feedback-regulated star formation, as discussed by [Ostriker et al. \(2010\)](#) and [Ostriker & Kim \(2022\)](#). Also, as stated in Eq. (13), we can infer it from the relationship between pressure and molecular gas surface density. Here we show that the linear relation between pressure and surface density of star formation naturally arises from basic principles.

The star formation rate per unit area should be proportional to Σ_{sg}/t_{ff} , where $t_{ff} = (32G\rho_{cl}/3\pi)^{-1/2}$ is the free fall time and ρ_{cl} is the average volume mass density of a cloud bounded by pressure and at the beginning of self-gravity. This average volume mass density is as before $\rho_{cl} = \mu P_{ISM}/(6 kT_{eff})$, and the free fall time for the parameters of our system is

$$t_{ff} \sim 7 \left(\frac{P_{ISM}}{P_\odot} \right)^{1/2} T_{100}^{-1/2} \text{ Myr.} \quad (37)$$

Theoretical and observational work have suggested that the entire life cycle of star-forming molecular clouds, from the time of their formation out from the CNM to their disruption by stellar feedback, lasts some $\sim 10 - 30$ Myr and between $10 - 15$ Myr for recent extragalactic estimates (see, e.g., [Blitz et al. 2007](#); [Fukui & Kawamura 2010](#); [Colín et al. 2013](#); [Vázquez-Semadeni et al. 2019](#); [Chevance et al. 2020, 2023](#)). The corresponding timescale for individual cloud clumps, or small clouds in the solar neighborhood, is smaller, on the order of $5 - 10$ Myr ([Leisawitz et al. 1989](#); [Ballesteros-Paredes et al. 1999b](#); [Hartmann et al. 2001](#); [Ballesteros-Paredes & Hartmann 2007](#)), and this range of values is expected for self-gravitating cores. Assuming t_{ff} as the lifetime of our self-gravitating structures, the resulting star formation rate per unit surface can be written as

$$\Sigma_{SFR} \approx \delta_a \frac{\Sigma_{sg}}{t_{ff}} \approx \delta_a 4 \left(\frac{P_{ISM}}{P_\odot} \right) T_{100}^{-1/2} M_\odot \text{ kpc}^{-2} \text{ yr}^{-1}, \quad (38)$$

where the proportionality factor δ_a corresponds to the fractional area subtended by star formation sites per kpc⁻².

As stated in Sect. (2.2), from the value of Eq. (13) at the solar circle one readily gets $\delta_a \sim 4 \times 10^{-4} T_{100}^{1/2}$ which, as we see below, represents a lower bound to $\Sigma_{SFR}(R_\odot)$. The upper bound can be estimated using the available molecular cloud data. The surface mass density of molecular gas in the solar circle is, as stated before, $\Sigma_{H_2}(R_\odot) \approx 1.5 M_\odot \text{ pc}^{-2}$, while the average mass of individual molecular clouds in Table 2 of [Miville-Deschénes et al. \(2017a\)](#) is about $1.5 \times 10^5 M_\odot$. Using the mass-radius relationship of the survey performed by [Roman-Duval et al. \(2010\)](#), $M_{cl} \approx 228 R_{cl}^{2.36} M_\odot$, where R_{cl} is the radius of the molecular cloud in pc, a cloud with $1.5 \times 10^5 M_\odot$ should have a radius of about 15 pc⁶. Thus, the effective area covered by each cloud complex, if round, is $\sim 7 \times 10^{-4} \text{ kpc}^2$.

⁶ This is a factor of 2 less than the average cloud size of [Miville-Deschénes et al. \(2017a\)](#). The high-resolution survey performed by [Roman-Duval et al. \(2010\)](#) provides better estimates of the clouds' sizes. Their Table 1 shows that clouds with masses around $10^5 M_\odot$ can have radii as small as 4 pc, but most of

The detailed census of the main molecular structures located within 2 kpc of the Sun performed by [Spilker et al. \(2021\)](#) shows that there are about six large molecular clouds per square kpc⁷. Then the fraction of the area covered in kpc² by these six clouds is $\sim 4 \times 10^{-3}$. Now, as already shown in Figure 3, a large fraction of molecular clouds between 6 and 10 kpc are not self-gravitating, and [Evans et al. \(2021a, 2022\)](#) found that only 17% to 19% of the CO mass in the MW is gravitationally bounded. Then, as a first approximation, we assume that the cover area of the self-gravitating structures is 0.18 of the area subtended by our six cloud complexes in the solar circle, resulting in $\delta_a \sim 7.6 \times 10^{-4}$. With this value, we get an upper bound for the pressure-regulated star formation rate per unit surface,

$$\Sigma_{\text{SFR}}(R) \approx 3 \times 10^{-3} \left(\frac{P_{\text{ISM}}}{P_{\odot}} \right) T_{100}^{-1/2} M_{\odot} \text{kpc}^{-2} \text{yr}^{-1}, \quad (39)$$

which, given the relationship between P_{ISM} and Σ_{H_2} (Eq. 12), can also be written in terms of the column density of molecular mass,

$$\Sigma_{\text{SFR}}(R) \approx 3 \times 10^{-3} \left[\frac{\Sigma_{H_2}}{\Sigma_{H_2}(R_{\odot})} \right] T_{100}^{-1/2} M_{\odot} \text{kpc}^{-2} \text{yr}^{-1}. \quad (40)$$

The values provided by these relationships and Eq. (13) are within the limits of the observational radial distributions compiled by [Misiriotis et al. \(2006\)](#); [Blitz & Rosolowsky \(2006\)](#); [Lee et al. \(2016\)](#); [Bacchini et al. \(2019\)](#); [Palla et al. \(2020\)](#) and [Soler et al. \(2023\)](#) for MW outside of 5 kpc, as shown in Figure 4. At the solar circle the observationally derived values are approximately $\Sigma_{\text{SFR}} \sim (1.5 - 5) \times 10^{-3} M_{\odot} \text{kpc}^{-2} \text{yr}^{-1}$ (note that the massive star tracers compiled by [Soler et al. \(2023\)](#) give larger values for the whole Galactic disk but these depend on the assumed IMF). The typical temperatures of molecular clouds range between 10 and 50 K ([Snow & McCall 2006](#)), using $T_{100} = 0.5$ as a representative value of the average temperature at the onset of self-gravity, Eq. (39) gives $\Sigma_{\text{SFR}} \sim 4 \times 10^{-3} M_{\odot} \text{kpc}^{-2} \text{yr}^{-1}$. Then, our upper and lower limits for the radial distribution of the surface density of the star formation rate in the MW can be written as,

$$\Sigma_{\text{SFR}} \sim (1.5 - 4) \times 10^{-3} \exp \left(\frac{R_{\odot} - R}{2 \text{kpc}} \right) M_{\odot} \text{kpc}^{-2} \text{yr}^{-1}, \quad (41)$$

which, within the data scatter, follows the radial trends observed between 5 and 12 kpc in the MW. Note that the slope is within the limits derived by [Lee et al. \(2016\)](#) for star formation in giant molecular cloud complexes, $\Sigma_{\text{SFR}} \propto \exp[-R/(1.7 \pm 0.3 \text{kpc})]$, and is also in line with the results of numerical simulations, using different virial parameters and CO conversion factors, discussed by [Evans et al. \(2022\)](#).

The resulting molecular gas depletion time for the MW disk is $t_{\text{dep}} = \Sigma_{H_2}/\Sigma_{\text{SFR}} \sim (1 - 0.4) \times 10^9 \text{ yr}$, but this is a lower limit because the molecular gas is replenishing from the CNM reservoir at the rate given in Section (3.4). With respect to star formation inside spiral arms, the arm-interarm pressure difference of a factor of 4 in the MW translates into a similar increase in the surface density of the star formation rate along the spiral arms. External galaxies show an average star formation contrast somewhat smaller, of a factor between 2 and 3 ([Querejeta et al. 2024b](#)).

A comparison of our rates with those obtained in nearby galaxies

them are close to 15 pc. Thus, the average values of [Miville-Deschénes et al. \(2017a\)](#) tend to overestimate cloud sizes and underestimate cloud densities.

⁷ The 3D dust maps recently studied by [Kormann et al. \(2025\)](#) display the presence of large wavelike gas structures in the solar neighborhood. These are corrugated, kiloparsec-sized atomic superclouds, which appear to be precursors for future giant molecular cloud complexes.

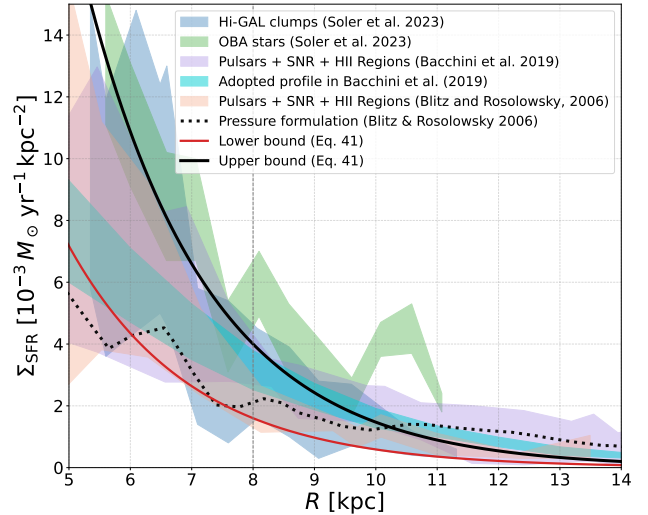


Figure 4. Radial profiles of the star formation rate surface density, Σ_{SFR} , as a function of Galactocentric radius. The solid curve represents the upper bound value in Eq. (41) and the solid red line represents the lower bound. The blue and green shaded regions correspond to data from Hi-GAL clumps and OBA stars, respectively (Soler et al. 2023, see their Figure B.1). The purple and beige regions represent estimates based on pulsars, supernova remnants, and HII regions, as reported by Bacchini et al. (2019) and Blitz & Rosolowsky (2006), respectively. The cyan region shows the adopted profile by Bacchini et al. (2019), while the dotted line is the prescription proposed by Blitz & Rosolowsky (2006).

in the EDGE-CALIFA survey by [Barrera-Ballesteros et al. \(2021\)](#) and the ALMaQUEST survey by [Ellison et al. \(2024\)](#) shows a very good agreement for star-forming regions with pressures below $\log(P_{\text{ISM}}/k) \sim 5.5$. In Figure 5 we show the upper and lower bounds of the rates predicted by our model in Eq. (41), superimposed on the contours that surround 90, 80, and 50% of the EDGE-CALIFA data obtained by [Barrera-Ballesteros et al. \(2021\)](#). Their best fit to the data, which is almost linear, lies very close to our upper bound.

4.3 The Star Formation Efficiency along the disk of the MW

The transformation of a molecular mass into stars is a very inefficient process and proceeds at different speeds in different places. This has been a recurrent topic, discussed over the years in observational and theoretical studies, and the efficiencies derived from observations range from about 40 % to a few percent ([Rydgren 1980](#); [Mathieu 1983](#); [Rengarajan 1984](#); [Franco & Shore 1984](#); [Elmegreen & Clemens 1985](#); [Franco et al. 1994](#); [Young et al. 1996](#); [Williams & McKee 1997](#); [Vázquez-Semadeni et al. 2003](#); [Zamora-Avilés et al. 2019a](#); [Wells et al. 2022](#); [Mattern et al. 2024](#)). For isolated clouds, the star formation efficiency is defined as $\epsilon_{\text{sf}}(t) = M_*(t)/M_0$, where $M_0 = M_g(t) + M_*(t)$ is the initial mass of the star-forming cloud and $M_*(t)$ and $M_g(t)$ are the mass of recently formed stars and the remaining gas mass at any time t , respectively. Star formation is zero at the moment of cloud formation, and the efficiency with which the molecular mass is transformed into stars increases as time progresses. The maximum efficiency value is achieved at the end of the lifetime of the parental cloud, when it is finally evaporated by the combined action of expanding HII regions, stellar winds, and SNe.

For the population of star-forming molecular clouds per unit area in a gaseous disk, the overall value of the final star formation efficiency

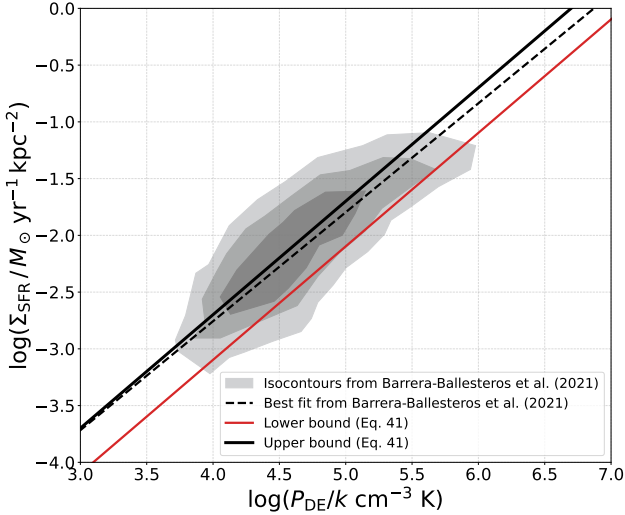


Figure 5. Comparison of the rates predicted by our model with the results of the EDGE-CALIFA survey (adapted from Fig. 9 in [Barrera-Ballesteros et al. 2021](#), graphed with the dynamic equilibrium pressure P_{DE} , see Sect. 2.1). The shaded contours enclose the 90, 80, and 50% data points of the sample and the dashed line represents their best fit. The solid curve is the upper bound value in Eq. (41) and the solid red line is the lower bound.

in equilibrium is simply the ratio of the gas mass transformed into stars per unit time and unit area, Σ_{SFR} , to the rate of mass that is destroyed from the molecular cloud reservoir, $\dot{\Sigma}_{\text{mol}}^-$,

$$\epsilon_{\text{sf}} = \frac{\Sigma_{\text{SFR}}}{\dot{\Sigma}_{\text{mol}}^-} \sim (3 - 8) \times 10^{-2}. \quad (42)$$

Therefore, for pressure-regulated star formation in the MW, the efficiency is nearly constant along the disk and is similar to the ones derived by [Franco et al. \(1994\)](#), [Federrath \(2016\)](#), and [Kim et al. \(2021\)](#) from cloud evaporation by photoionization and the combined effects of turbulence, magnetic fields, and stellar feedback. Recent studies with young stellar object counts at nearby star-forming sites indicate that the efficiency decreases with the mass of the parental cloud, and our derived value is appropriate for clouds with masses greater than $\sim 3 \times 10^3 M_{\odot}$, where the efficiency tends to an asymptotic value of about 8 % (see Figure 10 in [Wells et al. 2022](#), and references therein).

With respect to the efficiency of star formation per free fall time (see e.g., [Krumholz et al. 2005, 2012](#)), our pressure-regulated scheme gives values that depend on the square root of the pressure,

$$\epsilon_{\text{sf},\text{ff}} = \frac{\Sigma_{\text{SFR}}}{\Sigma_{H_2}} t_{\text{ff}} \sim (0.7 - 2) \times 10^{-2} \left(\frac{P_{\text{ISM}}}{P_{\odot}} \right)^{1/2} T_{100}^{-1/2}, \quad (43)$$

which are compatible with those found by [Kim et al. \(2021\)](#) and with the values generally quoted in the literature (see [Mattern et al. 2024](#), and references therein). The observationally derived values of $\epsilon_{\text{sf},\text{ff}}$ show large scatters, with mean values ranging from 0.3 % to 2.6 % (see [Utomo et al. 2018](#); [Mattern et al. 2024](#); [Leroy et al. 2025](#); [Meidt et al. 2025](#)). The scatter is much smaller for the specific case of luminous and ultraluminous IR galaxies, where [Wilson et al. \(2019\)](#) found larger but nearly constant mean values of 5% and 7%.

5 DISCUSSION

The interstellar pressure defines the properties of the gaseous components embedded in a galactic disk and is the substrate on which all physical and chemical interstellar processes occur, including those leading to molecular cloud formation and star formation. The velocity dispersion and temperature of the gas, its scale height, the mass exchange among the gas phases, and the destruction of star-forming clouds, on the other hand, are regulated by the energy input from young massive stars (e.g., [Field et al. 1969](#); [Cox & Smith 1974](#); [McKee & Ostriker 1977](#); [Cox 1983](#); [Franco & Shore 1984](#); [Parravano 1988, 1989](#); [Elmegreen 1989](#); [Elmegreen & Parravano 1994](#); [Wolfire et al. 2003](#); [Blitz & Rosolowsky 2006](#); [Ostriker et al. 2010](#); [Colín et al. 2013](#); [Elmegreen & Elmegreen 2019](#); [Grudić et al. 2021](#); [Ostriker & Kim 2022](#)). Thus, interstellar pressure and star formation are intimately intertwined to keep the system stirred and in a self-regulated state. Our simplified model emphasizes the main physical processes that participate in their entanglement and provides the pressure-regulated rates that maintain equilibrium along the gaseous disk.

The combined effects of differential rotation, supernova explosions, stellar radiation, and stellar winds drive the interstellar medium to form a network of gas flows across a wide range of scales. These flows easily develop internal interactions and can induce density fluctuations and hydrodynamical, thermal, and gravitational instabilities leading to the formation of molecular clouds and then to stars, but the conditions for each successive step towards star formation are different. In particular, for metallicities greater than $0.2 Z_{\odot}$, the total column density required for the transition from a cold atomic cloud to a molecular cloud is approximately $2\Sigma_d \sim 10 (Z/Z_{\odot})^{-1} M_{\odot} \text{ pc}^{-2}$, which is equivalent to $\log N_H \approx 21 + \log(Z_{\odot}/Z)$. Aside from the solar neighborhood, this metallicity dependence is also appropriate to explain the observed gas column densities for the atomic-molecular transition regions in the Magellanic Clouds, where the average metallicities are $Z_{\text{LMC}} \sim 0.5 Z_{\odot}$ and $Z_{\text{SMC}} \sim 0.2 Z_{\odot}$ (e.g., [Roman-Duval et al. 2022a](#)), and the FUV studies indicate $\log (N_H)_{\text{LMC}} \sim 21.3$ and $\log (N_H)_{\text{SMC}} \sim 22$ (see [Shull et al. 2021](#), and references therein). For the onset of internal gravitational instabilities, on the other hand, clouds must reach a column density of at least $\Sigma_{\text{sg}} \sim 30 (P_{\text{ISM}}/P_{\odot})^{1/2} M_{\odot} \text{ pc}^{-2}$. As is evident, the prerequisites for self-gravity and molecular cloud formation are different, but at the end, both are pressure-regulated.

Our pressure-regulated scheme is in line and complements previous ideas on the role of interstellar pressure in regulating the properties of the gas and the star formation process (e.g., [Elmegreen 1993b](#); [Elmegreen & Parravano 1994](#); [Wong & Blitz 2002](#); [Blitz & Rosolowsky 2004, 2006](#); [Ostriker et al. 2010](#); [Wilson et al. 2019](#); [Ostriker & Kim 2022](#)), and it can also be applied to a wide variety of different galactic environments as long as the metallicity is greater than $0.2 Z_{\odot}$ and the system pressure is below $\log(P_{\text{ISM}}/k) \sim 5.5$. This is evident in the comparison with the results of the EDGE-CALIFA survey ([Barrera-Ballesteros et al. 2021](#)) shown in Figure 5, which contains 4260 star-forming regions. These regions are distributed at different galactocentric radii along the disks of 96 nearby galaxies and have diverse local conditions with varied interstellar pressures, metallicities, gas velocity dispersions, radiation fields and cosmic ray fluxes. The upper limit of Equation 41 lies very close to the best fit of the observational results, but both limits of the equation are within the range of observed values. In future work, we will address additional details of some of the observed properties. The pressure dependence derived in different studies varies somewhat, but is always close to unity for systems with low pressure. On the

observational side, (Blitz & Rosolowsky 2006) found a slope of 0.92 for MW and nearby spirals, but Fisher et al. (2019) derived an exponent of 0.76 for the highly turbulent galaxies of the DYNAMO survey, and Molina et al. (2020) obtained an exponent close to 0.8 for starburst galaxies, while Barrera-Ballesteros et al. (2021) for the EDGE-CALIFA survey and Ellison et al. (2024) for the extended AL-MaQUEST sample got an almost linear exponent for systems with pressures below $\log(P/k) \sim 5.5$, and a shallower relation for pressures above this value. On the theoretical side Ostriker et al. (2010) constructed a pressure-regulated model assuming that the injection of energy from Σ_{SFR} should counterbalance the weight of the interstellar gas, and the results of the corresponding detailed numerical simulations by Kim et al. (2011) and Ostriker & Kim (2022) yield exponents close to 1.2. Krumholz et al. (2018) made a similar model but added gas inflows as an additional source of velocity dispersion and were able to get shallower relations at high rates of gas inflows that increase the interstellar pressures.

The model cannot be extended to the early phases of galaxy formation, but recent high-resolution hydrodynamic N-body simulations for galaxy formation are reaching parsec-size cell resolutions (Bland-Hawthorn et al. 2024, 2025). This level of detail for possible MW progenitors, which is not necessarily achieved in cosmological hydrodynamical simulations, indicates that stellar feedback and gas pressure are coupled and also act in concert during the strong initial episodes of halo accretion and star formation. This coupling not only increases the velocity dispersion of newly formed stars but together with gravitational and shear instabilities in the nascent disk also drives bulk motions that shake the gas and stellar components, eventually leading to the formation of the stellar bar and the old stellar disk in the Milky Way progenitors. The possible importance of our work in this area lies in providing a robust phenomenological framework that can be easily implemented in such large simulated volumes, which can resolve the physics of molecular clouds in galaxy evolution simulations.

For present-day conditions in the MW and spiral galaxies, dense clouds are typically formed through compressive events (Hartmann et al. 2001; Vázquez-Semadeni et al. 2007), and once a cloud becomes self-gravitating, it undergoes hierarchical collapse (Vázquez-Semadeni et al. 2019, and references therein). Consequently, the star formation rate must scale with the collapse rate (see, e.g., Ballesteros-Paredes et al. 2024), yielding the relation $\Sigma_{SFR} \propto \Sigma_g/t_{sf}$, where t_{sf} is the time it takes for a cloud to form stars, as several authors have discussed earlier (e. g. Larson 1992; Wong & Blitz 2002; Heiderman et al. 2010; Krumholz & Dekel 2012). In our case, we restricted the participating gas mass at the onset of self-gravity to Σ_{sg} and the time scale to t_{ff} , also at the onset of self-gravity. Note that our choice of time scale is in accordance with recent observational results in dense clouds. This fundamental dependence, assuming that self-gravitating clouds collapse on a free-fall timescale, allows us to account for the radial variation of the Milky Way's star formation rate. The absolute scaling of Σ_{SFR} , particularly at the solar circle, is here constrained using the results from Bigiel et al. (2008), to derive a lower limit, and by the filling factor of star-forming clouds per unit area in the galaxy, which can be constrained by observations (e.g., Miville-Deschénes et al. 2017a; Roman-Duval et al. 2010; Evans et al. 2021a; Spilker et al. 2021) to obtain the upper limit. Our upper limit values are almost in agreement with the best fit to the data of the EDGE-CALIFA survey derived by Barrera-Ballesteros et al. (2021).

In summary, metallicity defines the threshold condition for molecular clouds to form, and interstellar pressure sets the criterion for the onset of self-gravity. Once gravity takes over, the clouds collapse locally in about a free fall time, forming stars that will destroy their

parental clouds, limiting the star formation process (e.g., Franco et al. 1994; Colín et al. 2013; Zamora-Avilés et al. 2019b; Grudić et al. 2021; Kim et al. 2018; Ostriker et al. 2010; Ostriker & Kim 2022). This scheme links the star formation rate with the gas pressure and is at the core of the global and hierarchical collapse scenario of molecular cloud evolution (Vázquez-Semadeni et al. 2007; Heitsch & Hartmann 2008; Ballesteros-Paredes et al. 2018; Vázquez-Semadeni et al. 2019).

6 CONCLUSIONS

Here we have presented a simplified analytical model, based on the ideas first introduced by FC86, of the thresholds for molecular cloud formation and their transformation into self-gravitating entities, which are the actual sites of star formation. The results of this work are as follows.

- (i) The onset of molecular cloud formation out of the diffuse CNM medium, as proposed by FC86, is mainly due to the opacity of the dust. For metallicities greater than $\sim 0.2 Z_\odot$, the external HI-H₂ transition layer has a column mass density mainly of atomic gas $\Sigma_d \sim 5 (Z_\odot/Z) M_\odot \text{ pc}^{-2}$.
- (ii) We derive a modified version of the hydrogen molecule formation rate on dust grains that scales linearly with P_{ISM} , $F \approx 3.16 \times 10^{-8} (P_{ISM}/P_\odot) T_{100}^{-1/2} \text{ yr}^{-1}$. Given the threshold condition of the previous point, this implies that molecular cloud formation is controlled by pressure and metallicity.
- (iii) The total surface mass density threshold for molecular cloud formation and for star formation in the MW and nearby galaxies have a coincidental value of approximately $\sim 5 - 15 M_\odot \text{ pc}^{-2}$, but they refer to completely different entities. The one for the appearance of molecular clouds refers to twice the column density of the mainly atomic envelope protecting the molecular interior, $2\Sigma_d$. The one for the onset of star formation refers to the minimum molecular mass column density required to be self-gravitating.
- (iv) The formation rate of H₂ per unit area along the MW disk is $\dot{\Sigma}_{mol}^+ \sim 5 \times 10^{-2} (P_{ISM}/P_\odot) T_{100}^{-1/2} M_\odot \text{ kpc}^{-2} \text{ yr}^{-1}$. Assuming equilibrium with the star formation rate, this is equal to the sum of the molecular mass transformed into stars plus the amount of molecular mass evaporated from the parental clouds due to the energy input from recently formed stars, per unit area and unit time, $\dot{\Sigma}_{mol}^-$.
- (v) The star formation process inside $\sim 11 \text{ kpc}$ follows a two-step path. First, a molecular cloud is formed out of cold neutral gas, and when it contracts or gathers more gaseous mass from the external medium, it becomes self-gravitating and then is able to form stars.
- (vi) The star formation rate per unit surface on the MW disk, $\Sigma_{SFR} \sim (1.6 - 4) \times 10^{-3} (P_{ISM}/P_\odot) M_\odot \text{ kpc}^{-2} \text{ yr}^{-1}$, is pressure regulated and scales equally well and linearly with the surface mass density of molecular hydrogen. This result is in very good agreement with the EDGE-CALIFA and ALMaQUEST surveys for $\log(P_{ISM}/k) \leq 5.5$. The corresponding star formation efficiency is $\epsilon_{sf} \sim (3 - 8) \times 10^{-2}$ and the efficiency per free fall time is $\epsilon_{sf,ff} \sim (0.7 - 2) \times 10^{-2} (P_{ISM}/P_\odot)^{1/2} T_{100}^{-1/2}$.

ACKNOWLEDGEMENTS

The authors thank Stan Kurtz, Sebastián Sánchez, Steve Shore and an anonymous referee for very useful comments and suggestions that helped us to improve the present work. JF acknowledges many lively and informative discussions on these topics and over the years

with Don Cox, Gilberto Gómez, Tom Hartquist, Gerhard Hensler, Jong Soo Kim, Francesca Matteucci, Ron Reynolds, Sergei Silich, and Enrique Vazquez-Semadeni. ARP acknowledges financial support from DGAPA-PAPIIT IN106924. JBP acknowledges financial support from the UNAM-DGAPA-PAPIIT IG101723 grant.

DATA AVAILABILITY

No new data was generated during the preparation of this paper.

REFERENCES

Abgrall H., Le Bourlot J., Pineau Des Forets G., Roueff E., Flower D. R., Heck L., 1992, *A&A*, **253**, 525

Aoyama S., Hirashita H., Nagamine K., 2020, *MNRAS*, **491**, 3844

Arellano-Córdova K. Z., Esteban C., García-Rojas J., Méndez-Delgado J. E., 2021, *MNRAS*, **502**, 225

Armillotta L., Ostriker E. C., Jiang Y.-F., 2021, *ApJ*, **922**, 11

Asplund M., Grevesse N., Sauval A. J., Scott P., 2009, *ARA&A*, **47**, 481

Bacchini C., Fraternali F., Pezzulli G., Marasco A., Iorio G., Nipoti C., 2019, *A&A*, **632**, A127

Ballesteros-Paredes J., Hartmann L., 2007, *Rev. Mex. Astron. Astrofis.*, **43**, 123

Ballesteros-Paredes J., Vázquez-Semadeni E., Scalo J., 1999a, *ApJ*, **515**, 286

Ballesteros-Paredes J., Hartmann L., Vázquez-Semadeni E., 1999b, *ApJ*, **527**, 285

Ballesteros-Paredes J., Hartmann L. W., Vázquez-Semadeni E., Heitsch F., Zamora-Avilés M. A., 2011, *MNRAS*, **411**, 65

Ballesteros-Paredes J., Vázquez-Semadeni E., Palau A., Klessen R. S., 2018, *MNRAS*, **479**, 2112

Ballesteros-Paredes J., et al., 2024, *MNRAS*, **534**, 1043

Barrera-Ballesteros J. K., et al., 2021, *ApJ*, **909**, 131

Barreto-Mota L., de Gouveia Dal Pino E. M., Xu S., Lazarian A., 2024, *arXiv e-prints*, p. [arXiv:2405.12146](https://arxiv.org/abs/2405.12146)

Bienaymé O., et al., 2014, *A&A*, **571**, A92

Bigiel F., Leroy A., Walter F., Brinks E., de Blok W. J. G., Madore B., Thornley M. D., 2008, *AJ*, **136**, 2846

Bland-Hawthorn J., Tepper-Garcia T., Agertz O., Federrath C., 2024, *ApJ*, **968**, 86

Bland-Hawthorn J., et al., 2025, *arXiv e-prints*, p. [arXiv:2502.01895](https://arxiv.org/abs/2502.01895)

Blitz L., Rosolowsky E., 2004, *ApJL*, **612**, L29

Blitz L., Rosolowsky E., 2006, *ApJ*, **650**, 933

Blitz L., Fukui Y., Kawamura A., Leroy A., Mizuno N., Rosolowsky E., 2007, in Reipurth B., Jewitt D., Keil K., eds, *Protostars and Planets V*. p. 81 ([arXiv:astro-ph/0602600](https://arxiv.org/abs/astro-ph/0602600)), doi:10.48550/arXiv.astro-ph/0602600

Bohlin R. C., Savage B. D., Drake J. F., 1978, *ApJ*, **224**, 132

Boissier S., Boselli A., Buat V., Donas J., Milliard B., 2004, *A&A*, **424**, 465

Bonnell I. A., Dobbs C. L., Smith R. J., 2013, *MNRAS*, **430**, 1790

Boulares A., Cox D. P., 1990, *ApJ*, **365**, 544

Bovy J., Rix H.-W., 2013, *ApJ*, **779**, 115

Browning M. K., Tumlinson J., Shull J. M., 2003, *ApJ*, **582**, 810

Brugaletta V., et al., 2025, *MNRAS*, **537**, 482

Buat V., Deharveng J. M., Donas J., 1989, *A&A*, **223**, 42

Cheng X., Anguiano B., Majewski S. R., Arras P., 2024, *MNRAS*, **527**, 959

Chevance M., et al., 2020, *Space Sci. Rev.*, **216**, 50

Chevance M., Krumholz M. R., McLeod A. F., Ostriker E. C., Rosolowsky E. W., Sternberg A., 2023, in Inutsuka S., Aikawa Y., Muto T., Tomida K., Tamura M., eds, *Astronomical Society of the Pacific Conference Series* Vol. 534, *Protostars and Planets VII*. p. 1 ([arXiv:2203.09570](https://arxiv.org/abs/2203.09570)), doi:10.48550/arXiv.2203.09570

Chiang I.-D., et al., 2021, *ApJ*, **907**, 29

Clark C. J. R., et al., 2018, *A&A*, **609**, A37

Clark C. J. R., Roman-Duval J. C., Gordon K. D., Bot C., Smith M. W. L., Hagen L. M. Z., 2023, *ApJ*, **946**, 42

Colín P., Vázquez-Semadeni E., Gómez G. C., 2013, *MNRAS*, **435**, 1701

Collins J. A., Rand R. J., Duric N., Walterbos R. A. M., 2000, *ApJ*, **536**, 645

Commerçon B., Marcowith A., Dubois Y., 2019, *A&A*, **622**, A143

Cox D. P., 1983, *ApJL*, **265**, L61

Cox D. P., 2005, *ARA&A*, **43**, 337

Cox D. P., Smith B. W., 1974, *ApJL*, **189**, L105

Crocker R. M., Krumholz M. R., Thompson T. A., 2021, *MNRAS*, **502**, 1312

De Cia A., Ledoux C., Mattsson L., Petitjean P., Srianand R., Gavignaud I., Jenkins E. B., 2016, *A&A*, **596**, A97

De Cia A., Ledoux C., Petitjean P., Savaglio S., 2018, *A&A*, **611**, A76

De Vis P., et al., 2019, *A&A*, **623**, A5

Dettmar R. J., 1990, *A&A*, **232**, L15

Dickey J. M., Lockman F. J., 1990, *ARA&A*, **28**, 215

Draine B. T., 1978, *ApJS*, **36**, 595

Draine B. T., Bertoldi F., 1996, *ApJ*, **468**, 269

Draine B. T., et al., 2007, *ApJ*, **663**, 866

Dwek E., et al., 1995, *ApJ*, **445**, 716

Ellison S. L., et al., 2024, *MNRAS*, **527**, 10201

Elmegreen B. G., 1987, in Peimbert M., Jugaku J., eds, *IAU Symposium Vol. 115, Star Forming Regions*. pp 457–479

Elmegreen B. G., 1989, *ApJ*, **338**, 178

Elmegreen B. G., 1993a, *ApJ*, **411**, 170

Elmegreen B. G., 1993b, *ApJL*, **419**, L29

Elmegreen B. G., 2002, *ApJ*, **577**, 206

Elmegreen B. G., 2018, *ApJ*, **854**, 16

Elmegreen B. G., Clemens C., 1985, *ApJ*, **294**, 523

Elmegreen B. G., Elmegreen D. M., 2019, *ApJS*, **245**, 14

Elmegreen B. G., Parravano A., 1994, *ApJL*, **435**, L121

Evans Neal J. I., Heyer Marc-Antoine Miville-Deschénes M., Merello Q. N.-L. M., 2021a, *arXiv e-prints*, p. [arXiv:2107.05750](https://arxiv.org/abs/2107.05750)

Evans II N. J., Heyer M., Miville-Deschénes M.-A., Nguyen-Luong Q., Merello M., 2021b, *ApJ*, **920**, 126

Evans N. J., Kim J.-G., Ostriker E. C., 2022, *ApJL*, **929**, L18

Federman S. R., Glassgold A. E., Kwan J., 1979, *ApJ*, **227**, 466

Federrath C., 2013, *MNRAS*, **436**, 3167

Federrath C., 2016, *Journal of Plasma Physics*, **82**, 535820601

Federrath C., Klessen R. S., 2012, *ApJ*, **761**, 156

Federrath C., Klessen R. S., 2013, *ApJ*, **763**, 51

Feldmann R., 2015, *MNRAS*, **449**, 3274

Ferrière K. M., 2001, *Reviews of Modern Physics*, **73**, 1031

Field G. B., Goldsmith D. W., Habing H. J., 1969, *ApJL*, **155**, L149

Fisher D. B., et al., 2017, *MNRAS*, **464**, 491

Fisher D. B., Bolatto A. D., White H., Glazebrook K., Abraham R. G., Obreschkow D., 2019, *ApJ*, **870**, 46

Flannery B. P., Robege W., Rybicki G. B., 1980, *ApJ*, **236**, 598

Flynn C., Holmberg J., Portinari L., Fuchs B., Jahreiß H., 2006, *MNRAS*, **372**, 1149

Francis C., Anderson E., 2014, *MNRAS*, **441**, 1105

Franco J., Cox D. P., 1986, *PASP*, **98**, 1076

Franco J., Shore S. N., 1984, *ApJ*, **285**, 813

Franco J., Shore S. N., Tenorio-Tagle G., 1994, *ApJ*, **436**, 795

Franco J., Kim J., Alfaro E. J., Hong S. S., 2002, *ApJ*, **570**, 647

Freudenreich H. T., 1998, *ApJ*, **492**, 495

Fukui Y., Kawamura A., 2010, *ARA&A*, **48**, 547

Gao Y., Solomon P. M., 2004, *ApJS*, **152**, 63

Girichidis P., et al., 2016, *ApJL*, **816**, L19

Glassgold A. E., Langer W. D., 1974, *ApJ*, **193**, 73

Goldsmith P. F., 2013, *ApJ*, **774**, 134

Gómez G. C., Cox D. P., 2004, *ApJ*, **615**, 744

Gong M., Ostriker E. C., Wolfire M. G., 2017, *ApJ*, **843**, 38

Grenier I. A., Black J. H., Strong A. W., 2015, *ARA&A*, **53**, 199

Grudić M. Y., Guszejnov D., Hopkins P. F., Offner S. S. R., Faucher-Giguère C.-A., 2021, *MNRAS*, **506**, 2199

Gupta N., et al., 2025, *arXiv e-prints*, p. [arXiv:2504.00097](https://arxiv.org/abs/2504.00097)

Habing H. J., 1968, *Bull. Astron. Inst. Netherlands*, **19**, 421

Hamanowicz A., et al., 2024, *ApJ*, **966**, 80

Hartmann L., Ballesteros-Paredes J., Bergin E. A., 2001, *ApJ*, **562**, 852

Heiderman A., Evans II N. J., Allen L. E., Huard T., Heyer M., 2010, *ApJ*, **723**, 1019

Heitsch F., Hartmann L., 2008, *ApJ*, **689**, 290

Hollenbach D., McKee C. F., 1979, *ApJS*, **41**, 555

Hollenbach D., Salpeter E. E., 1971, *ApJ*, **163**, 155

Hoopes C. G., Sembach K. R., Heckman T. M., Meurer G. R., Aloisi A., Calzetti D., Leitherer C., Martin C. L., 2004, *ApJ*, **612**, 825

Hopkins P. F., et al., 2020, *MNRAS*, **492**, 3465

Hou K.-C., Aoyama S., Hirashita H., Nagamine K., Shimizu I., 2019, *MNRAS*, **485**, 1727

Issa M. R., MacLaren I., Wolfendale A. W., 1990, *A&A*, **236**, 237

Jenkins E. B., 2009, *ApJ*, **700**, 1299

Jenkins E. B., Tripp T. M., 2001, *ApJS*, **137**, 297

Jog C. J., Solomon P. M., 1984, *ApJ*, **276**, 127

Jura M., 1975a, *ApJ*, **197**, 575

Jura M., 1975b, *ApJ*, **197**, 575

Jura M., 1975c, *ApJ*, **197**, 581

Kalberla P. M. W., Dedes L., 2008, *A&A*, **487**, 951

Kalberla P. M. W., Haud U., 2018, *A&A*, **619**, A58

Kennicutt Jr. R. C., 1979, *ApJ*, **228**, 394

Kennicutt Robert C. J., 1989, *ApJ*, **344**, 685

Kennicutt Robert C. J., 1998, *The Astrophysical Journal*, **498**, 541

Kennicutt Robert C. J., De Los Reyes M. A. C., 2021, *ApJ*, **908**, 61

Kennicutt R. C., Evans N. J., 2012, *ARA&A*, **50**, 531

Khoperskov S. A., Vasiliev E. O., Sobolev A. M., Khoperskov A. V., 2013, *MNRAS*, **428**, 2311

Khoperskov S. A., Vasiliev E. O., Ladeyschikov D. A., Sobolev A. M., Khoperskov A. V., 2016, *MNRAS*, **455**, 1782

Kim W.-T., Ostriker E. C., 2002, *ApJ*, **570**, 132

Kim C.-G., Ostriker E. C., 2017, *ApJ*, **846**, 133

Kim W.-T., Ostriker E. C., Stone J. M., 2002, *ApJ*, **581**, 1080

Kim C.-G., Kim W.-T., Ostriker E. C., 2011, *ApJ*, **743**, 25

Kim J.-G., Kim W.-T., Ostriker E. C., 2018, *ApJ*, **859**, 68

Kim J.-G., Ostriker E. C., Filippova N., 2021, *ApJ*, **911**, 128

Kormann L. A., Alves J., Soler J. D., Pantaleoni González M., Swiggum C., Enßlin T. A., Edenhofer G., 2025, *arXiv e-prints*, p. arXiv:2507.14883

Kramer E. D., Randall L., 2016a, *ApJ*, **824**, 116

Kramer E. D., Randall L., 2016b, *ApJ*, **829**, 126

Krumholz M. R., Dekel A., 2012, *ApJ*, **753**, 16

Krumholz M. R., McKee C. F., 2005, *ApJ*, **630**, 250

Krumholz M. R., McKee C. F., Klein R. I., 2005, *Nature*, **438**, 332

Krumholz M. R., McKee C. F., Tumlinson J., 2008, *ApJ*, **689**, 865

Krumholz M. R., McKee C. F., Tumlinson J., 2009, *ApJ*, **699**, 850

Krumholz M. R., Dekel A., McKee C. F., 2012, *ApJ*, **745**, 69

Krumholz M. R., Burkhardt B., Forbes J. C., Crocker R. M., 2018, *MNRAS*, **477**, 2716

Larson R. B., 1992, *MNRAS*, **256**, 641

Lazarian A., Kowal G., Vishniac E., de Gouveia Dal Pino E., 2011, *Planet. Space Sci.*, **59**, 537

Lee S. M., Kim J., Franco J., Hong S. S., 2004, *Journal of Korean Astronomical Society*, **37**, 249

Lee E. J., Miville-Deschénes M.-A., Murray N. W., 2016, *ApJ*, **833**, 229

Leisawitz D., Bash F. N., Thaddeus P., 1989, *ApJS*, **70**, 731

Leroy A. K., Walter F., Brinks E., Bigiel F., de Blok W. J. G., Madore B., Thornley M. D., 2008, *AJ*, **136**, 2782

Leroy A. K., et al., 2025, *ApJ*, **985**, 14

Li Y., Mac Low M.-M., Klessen R. S., 2005, *ApJL*, **620**, L19

Love S. G., Joswiak D. J., Brownlee D. E., 1994, *Icarus*, **111**, 227

Madore B. F., van den Bergh S., Rogstad D. H., 1974, *ApJ*, **191**, 317

Maillard V., Bron E., Le Petit F., 2021, *A&A*, **656**, A65

Marasco A., Fraternali F., van der Hulst J. M., Oosterloo T., 2017, *A&A*, **607**, A106

Martin C. L., Kennicutt Robert C. J., 2001, *ApJ*, **555**, 301

Martos M. A., Cox D. P., 1998, *ApJ*, **509**, 703

Martos M., Allen C., Franco J., Kurtz S., 1999, *ApJL*, **526**, L89

Mata-Chávez M. D., Velázquez H., Pichardo B., Valenzuela O., Roca-Fábriga S., Hernández-Toledo H., Aquino-Ortíz E., 2019, *ApJ*, **876**, 6

Mathieu R. D., 1983, *ApJL*, **267**, L97

Mattern M., et al., 2024, *A&A*, **688**, A163

Mattsson L., Andersen A. C., 2012, *MNRAS*, **423**, 38

McGaugh S. S., Lelli F., Schombert J. M., 2016, *Phys. Rev. Lett.*, **117**, 201101

McKee C. F., Krumholz M. R., 2010, *ApJ*, **709**, 308

McKee C. F., Ostriker J. P., 1977, *ApJ*, **218**, 148

McKee C. F., Parravano A., Hollenbach D. J., 2015, *ApJ*, **814**, 13

Meidt S. E., et al., 2025, *arXiv e-prints*, p. arXiv:2505.19832

Misiriotis A., Xilouris E. M., Papamastorakis J., Boumis P., Goudis C. D., 2006, *A&A*, **459**, 113

Miville-Deschénes M.-A., Murray N., Lee E. J., 2017a, *Astrophys. J.*, **834**, 1

Miville-Deschénes M.-A., Murray N., Lee E. J., 2017b, *ApJ*, **834**, 57

Molina J., et al., 2020, *A&A*, **643**, A78

Mosenkov A. V., Savchenko S. S., Smirnov A. A., Camps P., 2021, *MNRAS*, **507**, 5246

Muñoz-Mateos J. C., et al., 2009, *ApJ*, **701**, 1965

Navarro J. F., Frenk C. S., White S. D. M., 1997, *ApJ*, **490**, 493

Neufeld D. A., et al., 2024, *ApJ*, **973**, 143

Ostriker E. C., Kim C.-G., 2022, *ApJ*, **936**, 137

Ostriker E. C., McKee C. F., Leroy A. K., 2010, *ApJ*, **721**, 975

Padoa P., Haugbølle T., Nordlund Å., 2012, *ApJL*, **759**, L27

Palla M., Matteucci F., Spitoni E., Vincenzo F., Grisoni V., 2020, *MNRAS*, **498**, 1710

Park G., et al., 2023, *ApJ*, **955**, 145

Parravano A., 1988, *A&A*, **205**, 71

Parravano A., 1989, *ApJ*, **347**, 812

Péroux C., Howk J. C., 2020, *ARA&A*, **58**, 363

Pineda J. L., Langer W. D., Velusamy T., Goldsmith P. F., 2013, *A&A*, **554**, A103

Ptuskin V. S., Moskalenko I. V., Jones F. C., Strong A. W., Zirakashvili V. N., 2006, *ApJ*, **642**, 902

Querejeta M., et al., 2024a, *A&A*, **687**, A293

Querejeta M., et al., 2024b, *A&A*, **687**, A293

Reid M. J., et al., 2019, *ApJ*, **885**, 131

Rémy-Ruyer A., et al., 2014, *A&A*, **563**, A31

Renaud F., et al., 2013, *MNRAS*, **436**, 1836

Rengarajan T. N., 1984, *ApJ*, **287**, 671

Reynolds R. J., 1993, in Holt S. S., Verter F., eds, American Institute of Physics Conference Series Vol. 278, Back to the Galaxy. AIP, pp 156–165, doi:10.1063/1.44005

Reynolds R. J., Roesler F. L., Scherb F., 1977, *ApJ*, **211**, 115

Rodríguez Montero F., Martin-Alvarez S., Slyz A., Devriendt J., Dubois Y., Sijacki D., 2024, *MNRAS*, **530**, 3617

Röllig M., et al., 2007, *A&A*, **467**, 187

Röllig M., Szczerba R., Ossenkopf V., Glück C., 2013, *A&A*, **549**, A85

Roman-Duval J., Jackson J. M., Heyer M., Rathborne J., Simon R., 2010, *Astrophys. J.*, **723**, 492

Roman-Duval J., et al., 2022a, *ApJ*, **928**, 90

Roman-Duval J., et al., 2022b, *ApJ*, **935**, 105

Romano D., Matteucci F., Salucci P., Chiappini C., 2000, *ApJ*, **539**, 235

Ryan-Weber E. V., et al., 2004, *AJ*, **127**, 1431

Rydgren A. E., 1980, *AJ*, **85**, 444

Sánchez S. F., 2020, *ARA&A*, **58**, 99

Sanduleak N., 1969, *AJ*, **74**, 47

Savage B. D., Bohlin R. C., Drake J. F., Budich W., 1977, *ApJ*, **216**, 291

Schaye J., 2004, *ApJ*, **609**, 667

Schinnerer E., Leroy A. K., 2024, *ARA&A*, **62**, 369

Schmidt M., 1959, *ApJ*, **129**, 243

Seta A., McClure-Griffiths N. M., 2025, *MNRAS*, **539**, 1024

Shull J. M., Danforth C. W., Anderson K. L., 2021, *ApJ*, **911**, 55

Skillman E. D., 1987, in Lonsdale Persson C. J., ed., NASA Conference Publication Vol. 2466, NASA Conference Publication. pp 263–266

Snow T. P., McCall B. J., 2006, *ARA&A*, **44**, 367

Soler J. D., et al., 2023, *A&A*, **678**, A95

Spilker A., Kainulainen J., Orkisz J., 2021, *A&A*, **653**, A63

Spitzer Jr. L., 1942, *ApJ*, **95**, 329

Sternberg A., Le Petit F., Roueff E., Le Bourlot J., 2014, *ApJ*, **790**, 10

Sun J., et al., 2020, *ApJ*, **892**, 148

Sun J., et al., 2023, *ApJL*, **945**, L19

Talbot R. J. J., 1980, *ApJ*, **235**, 821

Tielens A. G. G. M., Hollenbach D., 1985, *ApJ*, **291**, 722

Toomre A., 1964, [ApJ, 139, 1217](#)

Tumlinson J., et al., 2002, [ApJ, 566, 857](#)

Urquhart J. S., et al., 2025, [MNRAS, 539, 3105](#)

Utomo D., et al., 2018, [ApJL, 861, L18](#)

Vale Asari N., Stasińska G., 2021, in Storchi Bergmann T., Forman W., Overzier R., Riffel R., eds, IAU Symposium Vol. 359, Galaxy Evolution and Feedback across Different Environments. pp 371–380 ([arXiv:2005.06054](#)), doi:10.1017/S1743921320002124

Vázquez-Semadeni E., Ballesteros-Paredes J., Klessen R. S., 2003, [ApJL, 585, L131](#)

Vázquez-Semadeni E., Gómez G. C., Jappsen A. K., Ballesteros-Paredes J., González R. F., Klessen R. S., 2007, [ApJ, 657, 870](#)

Vázquez-Semadeni E., Palau A., Ballesteros-Paredes J., Gómez G. C., Zamora-Avilés M., 2019, [MNRAS, p. 2348](#)

Vílchez J. M., Relaño M., Kennicutt R., De Looze I., Mollá M., Galametz M., 2019, [MNRAS, 483, 4968](#)

Voshchinnikov N. V., Il'in V. B., Henning T., Dubkova D. N., 2006, [A& A, 445, 167](#)

Wells M. R. A., Urquhart J. S., Moore T. J. T., Browning K. E., Ragan S. E., Rigby A. J., Eden D. J., Thompson M. A., 2022, [MNRAS, 516, 4245](#)

Williams J. P., McKee C. F., 1997, [ApJ, 476, 166](#)

Wilson C. D., Elmegreen B. G., Bemis A., Brunetti N., 2019, [ApJ, 882, 5](#)

Wiseman P., Schady P., Bolmer J., Krühler T., Yates R. M., Greiner J., Fynbo J. P. U., 2017, [A& A, 599, A24](#)

Wolfire M. G., McKee C. F., Hollenbach D., Tielens A. G. G. M., 2003, [ApJ, 587, 278](#)

Wolfire M. G., Tielens A. G. G. M., Hollenbach D., Kaufman M. J., 2008, [ApJ, 680, 384](#)

Wong T., Blitz L., 2002, [ApJ, 569, 157](#)

Young J. S., Allen L., Kenney J. D. P., Lesser A., Rownd B., 1996, [AJ, 112, 1903](#)

Zafar T., Watson D., 2013, [A& A, 560, A26](#)

Zamora-Avilés Manuel & Vázquez-Semadeni E., 2014, [ApJ, 793, 84](#)

Zamora-Avilés M., et al., 2019a, [MNRAS, 487, 2200](#)

Zamora-Avilés M., Ballesteros-Paredes J., Hernández J., Román-Zúñiga C., Lora V., Kounkel M., 2019b, [MNRAS, 488, 3406](#)

Zhu Z., Shen M., 2013, in de Grijs R., ed., IAU Symposium Vol. 289, Advancing the Physics of Cosmic Distances. pp 444–447, doi:10.1017/S1743921312021928

Zhukovska S., Dobbs C., Jenkins E. B., Klessen R. S., 2016, [ApJ, 831, 147](#)

Zoccali M., Valenti E., 2024, [arXiv e-prints, p. arXiv:2412.01607](#)

de Jong T., Boland W., Dalgarno A., 1980, [A& A, 91, 68](#)

von Steiger R., Zurbuchen T. H., 2016, [ApJ, 816, 13](#)

This paper has been typeset from a $\text{\TeX}/\text{\LaTeX}$ file prepared by the author.